Noncollinear magnetic orders in PtFePt and PtMnPt stripes tailored by external electric fields: First-principles interactions and model energy landscapes

David Gallina,* Byungryul Jang, and G. M. Pastor
Institut für Theoretische Physik, Universität Kassel, Heinrich-Plett-Straße 40, 34132 Kassel, Germany

(Received 26 May 2025; revised 28 November 2025; accepted 21 January 2026; published 9 February 2026)

The stable and metastable magnetic orders in one-dimensional PtFePt and PtMnPt stripes, as well as the collective spin reorientations connecting them, are investigated by combining first-principles electronic theory with a detailed characterization of the associated energy landscapes. The relative stability of collinear and noncollinear magnetic orders is determined within density-functional theory by computing the frozen-magnon dispersion relations $\varepsilon^{\alpha}_{\delta\gamma}(q)$ as functions of wave number q, spin-polarization plane $\delta\gamma$, and chirality $\alpha = \pm 1$. The effective interactions between the local magnetic moments $\boldsymbol{\mu}_i$ at the $3d$ transition metal atoms are derived, including the local magnetic anisotropy energies K^{δ}_i, the symmetric exchange couplings J^{δ}_{ij}, and the Dzyaloshinskii-Moriya (DM) vectors $\boldsymbol{D}_{ij}$, where $\delta = x, y, z$ denotes the direction relative to the stripe geometry. The consequences of applying an external electric field (EF) on the magnetic couplings are quantified. Significant DM interactions are triggered by the EF, which breaks the inversion symmetry of the stripes. First-nearest-neighbor DM coupling dominates in ferromagnetic PtFePt, whereas second-nearest-neighbor DM coupling dominates in antiferromagnetic PtMnPt. The magnetic energy landscapes of the corresponding classical spin Hamiltonians $H[\boldsymbol{\mu}_i]$ are systematically explored without imposing any constraints on the orientations of $\boldsymbol{\mu}_i$. The metastable magnetic configurations involve domain walls (DWs) superimposed on the ferromagnetic (PtFePt) or antiferromagnetic (PtMnPt) backgrounds, whose width can be tuned by the applied EF. The morphology of the transition states and the minimum-energy paths connecting the local minima reveal the mechanisms for the creation, annihilation, and translation of magnetic domains (MDs). One observes that MDs with walls of opposite chirality, yielding a total winding number $\eta_z = 0$, identical to that of the ground state, are unstable, whereas domains with walls of the same chirality and $\eta_z = \pm 1$ are stabilized by significant energy barriers. Extremely small upper bounds for the energy barriers associated with domain-wall translations along the stripes are found, implying remarkably high mobility. The roles of the microscopic interactions K^{δ}_i, J^{δ}_{ij}, and $\boldsymbol{D}_{ij}$ in the topological protection, energy barriers, and relative stability of magnetic configurations are disclosed. The present investigations may serve as a methodological blueprint for advancing our understanding of the local-environment dependence of interactions between magnetic moments, their role in collective responses and relaxation processes, and the energy landscapes that underlie the physics of magnetic low-dimensional systems and nanostructures.

DOI: 10.1103/vjz5-hfdr

I. INTRODUCTION

Low-dimensional magnetism remains, even after decades of intensive study, one of the key challenges in condensed-matter physics. The investigation of transition metal (TM) nanostructures, such as clusters, chains, wires, stripes, and thin films, has revealed a wide variety of remarkable behaviors, ultimately stemming from the strong environment dependence of itinerant-electron magnetism. In past years, considerable efforts have been devoted to understanding the magneto-anisotropic properties of these systems from both fundamental and technological perspectives. Indeed, characterizing magnetic anisotropy is particularly challenging, as it reflects the subtle interplay between electron delocalization, Coulomb interactions, and spin-orbit (SO) coupling. At the same time, controlling anisotropy offers multiple possibilities to tune and optimize the material behavior for specific applications. Early studies mainly focused on characterizing the magnetic anisotropy energy (MAE), i.e., the dependence of the ground-state energy and the finite-temperature free energy on the orientation of the magnetization relative to the lattice structure [1–21]. More recently, increasing attention has been paid to the anisotropy of the interactions between the local magnetic moments, as they define the shapes of the most stable magnetic configurations, their relative stability, and the dynamical response of the system to external stimuli such as currents, laser pulses, or applied fields [22–31]. Elucidating the microscopic origin of anisotropic magnetic interactions in low-dimensional systems is therefore of central importance in current magnetic material research.

Of particular interest in this context are the antisymmetric anisotropic couplings, known as Dzyaloshinskii-Moriya

*Contact author: gallina@uni-kassel.de

Published by the American Physical Society under the terms of the Creative Commons Attribution 4.0 International license. Further distribution of this work must maintain attribution to the author(s) and the published article's title, journal citation, and DOI.

(DM) interactions, which favor noncollinear magnetic orders with specific chiralities, including spin-density waves (SDWs), skyrmions, and other localized spin textures [22–38]. Several electronic mechanisms responsible for DM couplings have been previously identified, involving, for example, mediating nonmagnetic atoms, permanent dipole moments, or SO-induced spin currents [22,31,33,39–41]. Besides the possibilities of creating novel states of matter, the DM interactions are particularly interesting because of their strong sensitivity to the local environment of the interacting atoms. For instance, one can show that the DM interaction between two local moments vanishes if the middle point between them is a center of symmetry [33]. Consequently, changing the symmetry allows us to trigger DM couplings, which could stabilize noncollinear magnetic arrangements [30,31,42]. This opens up remarkable possibilities for tailoring magnetic order by manipulating sample parameters, for example, through capping, strain, temperature gradients, or external fields.

Among the available control methods, electric fields (EFs) offer a particularly promising route for steering the spin degrees of freedom, as their application is both reversible and energy efficient. For example, one would like to develop materials whose magnetic anisotropy can be tuned via external EFs in a way that faster and more efficient domain-wall injection and magnetization reversals become possible at weaker magnetic fields or currents. Experiments have already demonstrated that EFs can be used to control the magneto-anisotropic behavior of a wide range of materials, including the interface exchange bias in multiferroic laminates and the magnetization directions of nanomagnets [25,43–55]. Furthermore, theoretical studies have investigated EF effects on molecules, clusters, multilayers, and surface nanostructures [42,56–66]. These works have revealed a number of significant magneto-electric effects, such as EF-induced modifications of the frozen-magnon dispersion relations and Curie temperature in Fe and Co monolayers, EF-assisted nucleation and annihilation of magnetic skyrmions in Pd/Fe/Ir(111), changes in the energy barriers for the EF-assisted writing and deleting of skyrmions, or the nucleation of skyrmions in an ultrathin film with EF pulses [42,64–66]. Despite this progress, understanding the EF dependence of magnetic interactions and characterizing the consequences of tuning them on the collective behavior of low-dimensional nanostructures remain subjects of considerable importance for guiding the design and optimization of magnetic materials.

The main goals of the present investigations are twofold: First, we determine the dominant interactions between the magnetic moments in narrow wires and quantify how they are modified by external EFs, focusing on PtFePt and PtMnPt stripes as particularly interesting examples of ferromagnetic (FM) and antiferromagnetic (AF) one-dimensional (1D) systems. To this end, we perform first-principles calculations of the frozen-magnon dispersion relations within Hohenberg-Kohn-Sham's density-functional theory (DFT). Second, using the calculated magnetic interactions, we construct a classical spin Hamiltonian and systematically explore the energy landscapes (ELs) of the stripes as functions of the orientations of the local moments, without imposing any constraints on the magnetic ordering. This allows us to identify the stable and metastable magnetic configurations, quantify their stability, and characterize the collective spin reorientations connecting them.

The remainder of the paper is organized as follows. Section II presents the theoretical background. This includes classifying the two-body interactions between the local moments according to their different symmetries, specifying the main technical details of the electronic calculations from which the magnetic couplings are derived, and describing the methods used to characterize the energy landscapes as functions of the spin orientations. Results for PtFePt and PtMnPt stripes are presented and discussed in Secs. III and IV. In Sec. III, we focus on the dispersion relations for spiral SDWs and on the magnetic interactions derived from them by giving special attention to the chirality effects induced by the applied EF. In Sec. IV, the ground state and metastable magnetic configurations are identified together with the transition states connecting them. The role played by the different symmetric and antisymmetric interactions in the creation, annihilation, and translation of magnetic domains is analyzed. The importance of chirality as a source of topological protection of spin arrangements is discussed. Finally, Sec. V summarizes our conclusions.

II. THEORY

A. Magnetic interactions

Phenomenological spin models are remarkably useful for investigating the low-energy physics of magnetic materials with anisotropic competing interactions. Not only their transparency is very attractive from a theoretical perspective, but also their simplicity is appealing, since it allows a thorough characterization of the complex energy landscapes and dynamical processes as a function of the orientations of the local magnetic moments $\boldsymbol{\mu}_i$. From a physical perspective, the applicability of effective spin models to transition-metal systems, which actually display itinerant magnetism, requires that the local magnetic moments preserve their identity for arbitrary magnetic orders, at least in the energy range of physical interest. This is known to be the case when the local moments are strong (e.g., in Fe, Co, Mn, and Cr) but tends to fail in weak ferromagnets such as Ni, where the fluctuations of the size of the local moments and exchange splittings are known to be important [67–69]. The following results show that the local magnetic moments in PtFePt and PtMnPt stripes are particularly strong and almost independent of the magnetic order, even far away from the ground-state configuration. Furthermore, from a formal perspective, the local moment picture is justified by the functional-integral formulation of the spin-fluctuation theory of d-band and spd-band Hamiltonians [67,68]. These theoretical studies have been recently extended to describe the effects of spin-orbit interactions and temperature-dependent magnetic anisotropy in the framework of the first-principles methods and many-body models [18–21]. More recent examples of successful calculations and applications of classical spin models in the context of the magnetic anisotropy and chiral interactions of TM systems may be found in Refs. [24–31].

The effective pairwise interactions between the local magnetic moments $\boldsymbol{\mu}_i$ at the $3d$ TM atoms i are obtained by

expanding the total electronic energy to second order in their orientations $\hat{\boldsymbol{\mu}}_i = \boldsymbol{\mu}_i/|\boldsymbol{\mu}_i|$ [70]. The resulting quadratic approximation of the interaction energy takes the form of a classical spin Hamiltonian composed of four irreducible terms corresponding to different symmetries,

$$H = H_{\rm H} + H_{\rm SA} + H_{\rm LA} + H_{\rm DM}. \tag{1}$$

The rotational invariant part of the interactions is described by

$$H_{\rm H} = -\frac{1}{2}\sum_{i\neq j} J_{ij}\,\hat{\boldsymbol{\mu}}_i \cdot \hat{\boldsymbol{\mu}}_j, \tag{2}$$

where J_{ij} stands for the isotropic Heisenberg exchange coupling between atoms i and j. These couplings give a measure of the relative stability between parallel and antiparallel orientations of $\boldsymbol{\mu}_i$, irrespectively of their orientation with respect to the lattice structure. They usually define the largest energy scale in the model. The anisotropy of the exchange interactions is taken into account by the symmetric anisotropic term

$$H_{\rm SA} = -\frac{1}{2}\sum_{i\neq j} \hat{\boldsymbol{\mu}}_i \cdot \boldsymbol{\Delta J}_{ij}\,\hat{\boldsymbol{\mu}}_j, \tag{3}$$

where $\boldsymbol{\Delta J}_{ij}$ are traceless symmetric matrices. In lattice structures with high point-group symmetry (e.g., reflection symmetry across the xy, yz, and zx planes, as the ones considered in this paper) these matrices can be diagonalized simultaneously for all relevant pairs ij, i.e., $\Delta J_{ij}^{\gamma\delta} = \Delta J_{ij}^{\gamma}\delta_{\gamma\delta}$ with $\gamma, \delta = x$, y, and z. In this case, $H_{\rm SA}$ takes the simpler form

$$H_{\rm SA} = -\frac{1}{2}\sum_{i\neq j}\sum_{\gamma} \hat{\mu}_i^{\gamma}\,\Delta J_{ij}^{\gamma}\,\hat{\mu}_j^{\gamma}, \tag{4}$$

which we assume in the following. ΔJ_{ij}^{γ} represents the deviation in the exchange coupling between $\boldsymbol{\mu}_i$ and $\boldsymbol{\mu}_j$ with respect to the average J_{ij} when the local moments point along the direction γ. They are the consequence of SO interactions and are typically one or two orders of magnitude weaker than the isotropic J_{ij}.

The third term in Eq. (1) takes into account the local anisotropy energy

$$H_{\rm LA} = \sum_i \hat{\boldsymbol{\mu}}_i \cdot \boldsymbol{K}_i\,\hat{\boldsymbol{\mu}}_i, \tag{5}$$

where $\boldsymbol{K}_i$ are real symmetric matrices. In our case, $\boldsymbol{K}_i$ is diagonal and independent of i, so that this term can be written as

$$H_{\rm LA} = K^{\gamma}\sum_{i,\gamma}\left(\mu_i^{\gamma}\right)^2. \tag{6}$$

Together with the anisotropy of the exchange couplings, K^{γ} defines the magnetic anisotropy energy per atom $\Delta\mathcal{E}_{\gamma\delta}$, which represents the energy change upon uniformly rotating a collinear magnetic configuration along the δ direction (e.g., a FM or AF state) toward the γ direction. For example, in the FM case $\Delta\mathcal{E}_{\gamma\delta} = (K^{\gamma} - K^{\delta}) - \sum_j(\Delta J_{ij}^{\gamma} - \Delta J_{ij}^{\delta})/2$, where the sum runs over the neighbors j of some reference atom i.

Finally, the fourth term in Eq. (1) describes the antisymmetric anisotropic coupling between the local moments, usually known as the Dzyaloshinskii-Moriya (DM) interaction [32,33]. It is given by

$$H_{\rm DM} = \frac{1}{2}\sum_{i,j} \boldsymbol{D}_{ij}\cdot(\hat{\boldsymbol{\mu}}_i \times \hat{\boldsymbol{\mu}}_j), \tag{7}$$

where $\boldsymbol{D}_{ij} = -\boldsymbol{D}_{ji}$ are pseudovectors. While the previous symmetric terms are unaffected by exchanging the orientations of the magnetic moments at atoms i and j, the DM interaction does differentiate between magnetic configurations having opposite chiralities. Therefore, it defines the most favorable sense of rotation of $\boldsymbol{\mu}_i$ relative to $\boldsymbol{\mu}_j$ in noncollinear arrangements. Notice that the sign convention in Eq. (7) is such that the favored sense of rotation of the local magnetic moments, as we move from atom i to atom j, is the one in which $\hat{\boldsymbol{\mu}}_i$, $\hat{\boldsymbol{\mu}}_j$, and $\boldsymbol{D}_{ij}$ form a left-handed basis [i.e., $\boldsymbol{D}_{ij}\cdot(\hat{\boldsymbol{\mu}}_i \times \hat{\boldsymbol{\mu}}_j) < 0$]. We denote the clockwise chirality with $-$ and the counterclockwise chirality with $+$ (see Fig. 1). The magnitude of $\boldsymbol{D}_{ij}$ gives a measure of the relative stability between these magnetic configurations.

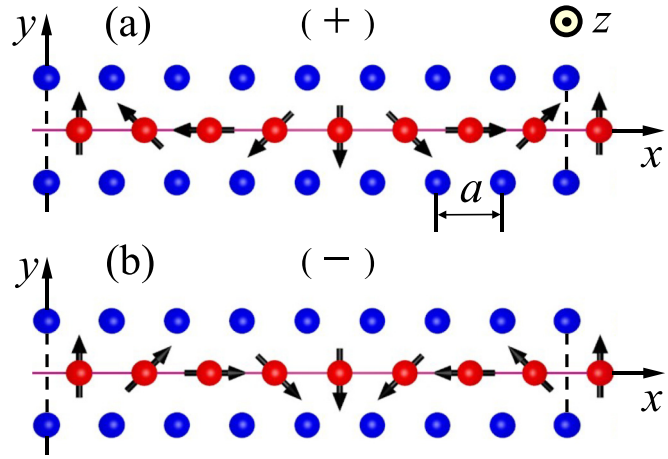


FIG. 1. Illustration of spiral spin-density waves in PtFePt or PtMnPt stripes with wave vector $\mathbf{q} = (0, 0, \pi/4)$ and (a) counterclockwise (+) or (b) clockwise (−) chirality. The arrows at the $3d$ TM atoms (red spheres) indicate the orientation of the local magnetic moments $\boldsymbol{\mu}_i$ within the xy plane. Pt atoms are represented by blue spheres. The supercell boundaries are marked by the vertical dashed lines.

The orientation of $\boldsymbol{D}_{ij}$ is largely defined by the point-group symmetry of the lattice around the bond connecting the atoms i and j. Applying the rules formulated by Moriya to the stripe structure shown in Fig. 1, one concludes that $\boldsymbol{D}_{ij} = 0$ for all pairs of $3d$ TM atoms i and j, since the stripes show inversion symmetry with respect to the points C_{ij} bisecting the segments $\boldsymbol{r}_{ij} = \boldsymbol{r}_j - \boldsymbol{r}_i$ [33]. However, this symmetry can be broken by applying an external field $\boldsymbol{E}$, which then triggers finite DM couplings. For example, for $\boldsymbol{E} = (0, E_y, 0)$ the DM vectors $\boldsymbol{D}_{ij} = (0, 0, D_{ij}^z)$ are perpendicular to the stripe plane, since the system is invariant upon reflections across the xy and yz planes passing through C_{ij} (see Fig. 1). Similarly, applying $\boldsymbol{E} = (0, 0, E_z)$ in the direction normal to the stripe plane would result in DM vectors of the form $\boldsymbol{D}_{ij} = (0, D_{ij}^y, 0)$ since the reflections across the yz and zx planes leave the system unchanged [33]. In the following, we focus on the effects

of electric fields along the y axis, which induce DM vectors perpendicular to the stripes, thus stabilizing spiral spin density waves with local moments within the stripe plane.

The classical spin Hamiltonian described above is employed in the following for two main purposes. First, it allows us to analyze the dependence of the electronic energy of the stripes on magnetic order from a local perspective by quantifying the effective interactions between local magnetic moments. Second, the simplicity of its pairwise-interaction form provides great flexibility for exploring arbitrarily complex magnetic arrangements and rearrangements, such as domain-wall formation, annihilation, and translation, which are inaccessible to first-principles methods. In this context, it is important to recall that the fundamental theoretical description of the stripes, from which the composition and local-environment dependence of the magnetic interactions are derived, remains a first-principles electronic theory that accounts for the itinerant character of transition-metal magnetism, as described in the following section.

B. Density-functional calculations

The interactions defining the spin Hamiltonian H in Pt-FePt and PtMnPt stripes are determined by calculating the frozen-magnon dispersion relations $\varepsilon^{\alpha}_{\gamma\delta}(q)$ within the framework of Hohenberg-Kohn-Sham's density-functional theory (DFT) [71,72]. We consider stripes lying in the xy plane and extending along the x axis as illustrated in Fig. 1. The lattice parameters are $a = 2.73$ Å with FePt distance $d_{\mathrm{FePt}} = 2.69$ Å for the PtFePt stripe, and $a = 2.80$ Å with MnPt distance $d_{\mathrm{MnPt}} = 2.76$ Å for the PtMnPt stripe. These values correspond to the nearest-neighbor (NN) distances in the $L1_0$ structure of the respective bulk alloys, as obtained from DFT geometry optimizations. Assuming for simplicity that all local moments lie within the same principal plane $\gamma\delta = xy$, yz, or zx, the spin-spiral states are defined by the wave vector $\boldsymbol{q} = (q, 0, 0)$ and the chirality $\alpha = \pm 1$, which specifies the sense of rotation of the magnetization density in noncollinear arrangements (see Fig. 1). The spin-wave total energies $\mathcal{E}^{\alpha}_{\gamma\delta}(q)$, from which $\varepsilon^{\alpha}_{\gamma\delta}(q)$ are derived, are calculated by constraining the direction of the local magnetic moment $\boldsymbol{\mu}_i$ at the $3d$ TM atoms i in a supercell containing N PtFePt or PtMnPt units. For each considered $N \leqslant 16$, one thus obtains $\mathcal{E}^{\alpha}_{\gamma\delta}(q)$ for the wave numbers compatible with the cell periodicity, i.e., $q = 2\pi l/Na$ with $0 \leqslant l < N$. The collinear FM and AF orders correspond to $q = 0$ and $q = \pi/a$, respectively. The supercell dimensions in the directions perpendicular to the stripe are at least 16 Å to avoid any spurious interactions between periodic replicas.

The DFT calculations of $\mathcal{E}^{\alpha}_{\gamma\delta}(q)$ have been performed using the Vienna *Ab initio* Simulation Package (VASP) [73,74]. The spin-polarized Kohn-Sham orbitals are expanded in an augmented plane-wave basis set, taking into account the interaction between valence electrons and ionic cores within the projector-augmented-wave approximation [75]. Exchange and correlation effects are described by means of the Perdew-Burke-Ernzerhof parametrization of the generalized-gradient approximation [76]. For each considered magnetic configuration (i.e., for given $\gamma\delta$, q, and α) the orientations of the local magnetic moments $\boldsymbol{\mu}_i$ are constrained by adding a penalty function to the Hohenberg-Kohn energy functional [77,78]. The local magnetic moments $\boldsymbol{\mu}_i$ are obtained by integrating the magnetization density $\boldsymbol{m}(\boldsymbol{r})$ within the Wigner-Seitz sphere Ω_i of atom i. Spin-orbit interactions are treated self-consistently by performing independent calculations for all considered wave vectors and spin-polarization planes. To this end, the method proposed by Lebacq and Kresse is employed [79,80]. Except for the constraints in the $3d$ moment directions, the electronic system is considered to be in the ground state. No restrictions are imposed on the spin density at the Pt atoms or on the moduli of the $3d$ moments. In this way, these electronic degrees of freedom are optimized, thus corresponding to the most stable solution of the Kohn-Sham equations for the given orientations $\hat{\boldsymbol{\mu}}_i$ [81,82].

The numerical convergence and stability of the calculations are ensured by considering fractional occupations of the Kohn-Sham orbitals with a Gaussian smearing $\sigma = 0.01$ eV. The resulting entropy of the occupation-number distribution is of the order 10^{-7} eV/K/atom. Concerning the expansion of the Kohn-Sham orbitals, a cutoff energy $E_{\mathrm{max}} = 500$ eV has been used for the plane-wave basis set. The number of k points in the Brillouin-zone sampling is $N_k = 120$. The selfconsistent calculations are pursued until the total-energy change between subsequent optimization steps is smaller than $E_{\mathrm{diff}} = 10^{-7}$ eV/atom. These numerical parameters have been verified to be sufficient for determining the energy differences relevant to this work, which are of the order of 10^{-4} eV/atom or larger [83].

The frozen-magnon dispersion relations for the different spin-polarization planes $\gamma\delta$ and chiralities α are given by the energy differences $\varepsilon^{\alpha}_{\gamma\delta}(q) = \mathcal{E}^{\alpha}_{\gamma\delta}(q) - \mathcal{E}_0(q_0)$, where the reference energy $\mathcal{E}_0(q_0)$ corresponds to the most stable wave number q_0 of the stripe along the easy magnetization direction. As discussed below, the ground states are collinear: $q_0 = 0$ for the ferromagnetic PtFePt stripes and $q_0 = \pi/a$ for the antiferromagnetic PtMnPt stripes. In this context, it is also useful to consider the MAE $\Delta\mathcal{E}_{\mu\nu}$ associated with rotating the collinear state with $q = q_0$ from the magnetization direction ν toward the direction μ ($\mu, \nu = x, y, z$). This is given by the corresponding total-energy difference $\Delta\mathcal{E}_{\mu\nu} = \mathcal{E}_{\mu}(q_0) - \mathcal{E}_{\nu}(q_0)$.

The effective interactions between the local magnetic moments and their anisotropies are obtained from a least-square fit of the dispersion relations calculated with DFT using the spin model H introduced in Eqs. (1)–(7) of Sec. II A. This model accounts for all different types of pairwise interactions (e.g., simple isotropic exchange couplings or including anisotropies) as well as different interactions ranges (e.g., up to first, second, or even more distant NNs). Since increasing the complexity of the model always reduces the standard deviation of any least-square fit, it is not obvious *a priori* how to choose the most appropriate physical model describing the first principles results. To achieve an optimum balance between reaching the highest fit quality and avoiding overfitting, we have applied the Akaike information criterion (AIC) [84,85]. Further details are given in the Appendix.

C. Metastable states and elementary transitions

The classical spin models derived from DFT calculations not only provide detailed insight into the nature of spin

couplings from a local perspective. They also enable a systematic study of the energy landscape (EL) of the system as a function of the orientations of the local magnetic moments, without imposing any constraints on the magnetic order. In this way, it is possible to unfold the properties of complex magnetic arrangements that are currently inaccessible to first principles methods.

The most important stationary points of an energy landscape are the local minima (LM), which represent the metastable states of the system, and the first-order saddle points or transition states (TS), which correspond to the lowest energy barrier along the boundary between the attraction basins of two nearby LM. The most probable pathway between two metastable states is the minimum energy path (MEP) that follows the gradient curve connecting the LM over one or several TS. In practice, the LM are obtained by using the conjugate gradient (CG) algorithm together with a backtracking line search employing the Armijo criterion [86–89]. Both are adapted to optimization on the product manifold $S(2)^N$ that is spanned by the orientations of the local moments in the supercell [90,91]. In the present study, cells containing up to $N = 200$ TM atoms have been considered. This is sufficient in practice, since the magnetic textures found in the low-energy configurations involve less than 100 TM atoms.

The TS connecting the LM are located using the nudged-elastic-band (NEB) algorithm [92]. In this method, the MEP between two metastable states is approximated by a discrete set or band of configurations $\vec{x}_l \in S(2)^N$ known as images (typically $m \simeq 9$). These images interact through artificial springs which keep the intermediate configurations evenly distributed along the path. To converge the band toward the MEP, each image $\vec{x}_l$ is optimized under the effect of two forces: the projection of the true energy gradient perpendicular to the path tangent at $\vec{x}_l$ and the tangential component of the artificial spring force [92,93]. Since the optimization takes place on $S(2)^N$, both the tangent vectors and forces are projected onto the linear space tangent to $S(2)^N$ at $\vec{x}_l$. A detailed description of the NEB method on spherical product manifolds may be found in Ref. [94]. The image with the highest energy generally lies quite close to the true TS, though it is often not fully converged. Therefore, in this work, the eigenvector following (EF) algorithm is subsequently used to accurately locate the TS. This method involves maximizing the energy along the unstable mode of the Hessian of the energy landscape, while minimizing the energy along all the directions perpendicular to it [95,96]. Finally, the configurations $\vec{x}$ defining the MEP are obtained by following the gradient curve starting from the TS, thus representing the lowest-energy evolution of the magnetic configurations between the local minima.

To follow the energy profile and magnetic configuration along the MEPs, we introduce the reaction coordinate $\lambda(\vec{x})$ whose absolute value is equal to the distance along the path in $S(2)^N$ between the configuration $\vec{x}$ and the ground state $\vec{x}_0$. The sign of λ is taken to be positive (negative) for MEPs leading to a metastable state with counterclockwise (clockwise) chirality $\alpha = \pm 1$. In practice, we discretize the path between $\vec{x}_0$ and $\vec{x}$ using a large number K of intermediate configurations $\vec{x}_l$ such that $\lambda(\vec{x})$ is accurately given by

$$\lambda(\vec{x}) = \alpha \left[\sum_{l=0}^{K} L(\vec{x}_l, \vec{x}_{l+1}) \right], \tag{8}$$

where $\vec{x}_{K+1} = \vec{x}$ and

$$L(\vec{y}, \vec{y}\,') = \sqrt{\sum_{i=1}^{N} \arccos[\hat{\boldsymbol{\mu}}_i(\vec{y}) \cdot \hat{\boldsymbol{\mu}}_i(\vec{y}\,')]^2}, \tag{9}$$

is the geodesic distance between the magnetic configurations $\vec{y}$ and $\vec{y}\,'$ in $S(2)^N$. In Eq. (9), $\hat{\boldsymbol{\mu}}_i(\vec{y})$ is the direction of the ith local moment in the configuration $\vec{y}$. Notice that λ is univocally defined once the size of the local moments $\hat{\boldsymbol{\mu}}_i$ is normalized to 1. As a natural unit, one may consider the path length involved in reversing a single spin, which is equal to π. The length of the path between critical points, for instance, between the ground state and the TS, provides a first measure of the complexity of the associated spin rearrangement.

III. MAGNETIC INTERACTIONS FROM FIRST PRINCIPLES

In this section, we determine the effective magnetic interactions between the local moments at the $3d$ TM atoms in PtFePt and PtMnPt stripes, which define the classical spin Hamiltonian introduced in Sec. II A. To this end, the stability of spin-density waves (SDWs) is quantified by calculating the frozen-magnon dispersion relations $\varepsilon^{\alpha}_{\gamma\delta}(q) = \mathcal{E}^{\alpha}_{\gamma\delta}(q) - \mathcal{E}_0(q_0)$ as a function of the wave number q along the stripe for different spin-polarization planes $\gamma\delta$ and chiralities α (see Fig. 1). The reference energy $\mathcal{E}_0(q_0)$ corresponds to the most stable magnetic configuration of the stripe, namely, the FM state with wave-number $q_0 = 0$ and easy magnetization direction $\gamma = y$ for the PtFePt stripes and the AF state with $q_0 = \pi/a$ and local moments along the easy axis $\gamma = x$ for the PtMnPt stripes.

A. PtFePt stripes

In Fig. 2, the magnon-dispersion relations $\varepsilon^{\alpha}_{\gamma\delta}(q)$ of PtFePt stripes are shown. The discrete points are derived from density functional supercell calculations, as described in Sec. III, whereas the curves correspond to the fits of the first-principles results using the classical spin model introduced in Sec. II A [71–76]. The magnetic interactions derived from the fits are reported in Table I. A strong stability of the FM order is observed. The q dependence of $\varepsilon^{\alpha}_{\gamma\delta}(q)$ is approximately proportional to $\cos(qa)$ for all spin-polarization planes, which indicates that the NN symmetric exchange couplings dominate [see Eq. (2)]. The same qualitative behavior is found regardless of whether an external electric field is applied [see Figs. 2(a) and 2(b)]. The anisotropies of the total energy and exchange interactions are derived by comparing the results for different magnetization directions and spin-polarization planes. In particular, we obtain that the easy magnetization direction is along the y axis, i.e., within the stripe plane and perpendicular to FePt interfaces.

The calculated MAEs per Fe atom in PtFePt stripes are $\Delta\mathcal{E}_{xy} = 3.5$ meV (3.8 meV) and $\Delta\mathcal{E}_{zy} = 5.9$ meV (5.8 meV)

TABLE I. Symmetric isotropic exchange interactions $J_{0\nu}$ and anisotropy of the symmetric interactions $\Delta J^{\gamma}_{0\nu}$, local anisotropy energies K^{γ}, and z component of the Dzyaloshinskii-Moriya vectors $D^{z}_{0\nu}$ between the local magnetic moments in one-dimensional PtFePt and PtMnPt stripes, where ν labels the neighbors of a reference $3d$ atom $i = 0$ in order of increasing distance and $\gamma = x, y, z$. See Eqs. (1)–(7). The values, given in meV, are obtained by fitting the density-functional results shown in Figs. 2 and 4. The uncertainties in the parameters, inherent to the least-square fits, are estimated to be 0.1–0.2 meV.

		J_{01}	ΔJ^{x}_{01}	ΔJ^{y}_{01}	ΔJ^{z}_{01}	J_{02}	ΔJ^{x}_{02}	ΔJ^{y}_{02}	ΔJ^{z}_{02}	K^{x}	K^{y}	K^{z}	D^{z}_{01}	D^{z}_{02}
PtFePt	$E_y = 0.5$ V/Å	78.4	2.7	–3.0	0.3	6.2	–2.1	3.5	–1.5	2.2	–4.7	2.6	–2.5	–0.2
	$E_y = 0$	81.3	3.4	–4.7	1.4	5.1	–0.5	0.5	0.0	2.4	–5.3	2.9	0.0	0.0
PtMnPt	$E_y = 0.5$ V/Å	–33.6	–4.9	1.5	3.4	4.2	2.8	–0.7	–2.2	–2.1	–2.2	4.3	–0.3	0.6
	$E_y = 0$	–33.3	–5.1	2.0	3.1	3.6	3.1	–1.2	–1.9	–2.3	–2.4	4.8	0.0	0.0

for an external field $E_y = 0.5$ V/Å ($E_y = 0$). They result from an interplay between the contributions of the local anisotropies K^{γ}, which favor magnetization along the y axis, and the anisotropy of the NN exchange couplings, which are stronger when the magnetization is along x and, to a lesser extent, along z (see Table I). These values are of the same order of magnitude as those found in free Fe chains [12]. This similarity is understandable, since PtFePt stripes and pure Fe stripes share the same reduced dimensionality and strong reduction of the local coordination number. Nevertheless, significant differences in both the sign and magnitude of the MAEs are also evident. They highlight the role of Pt atoms and illustrate the possibilities for tailoring magnetic anisotropy through $3d$-$5d$ alloying. The calculated local magnetic moments μ_i within the Wigner-Seitz spheres of the Fe atoms lie in the narrow range $\mu_{\mathrm{Fe}} = 3.41$–$3.44\,\mu_B$, being nearly independent of both wave number q and spin-polarization plane. This confirms the high stability of the local Fe moments resulting from strong intraatomic Coulomb interactions (Hund's first rule). It also supports the assumption that the energy landscapes of the stripes are functions of the orientations of the local Fe moments, as assumed in the spin model presented in Sec. II A. The magnetic moments induced at the Pt atoms, on which no constraints are imposed, show a much richer dependence on the magnetic order. Their magnitude decreases monotonically with increasing q, from $\mu_{\mathrm{Pt}} \simeq 0.4$–$0.5\,\mu_B$ in the FM ground state ($q = 0$), depending somewhat on the spin-polarization plane, to $\mu_{\mathrm{Pt}} \leqslant 0.05\,\mu_B$ for the AF configuration ($q = \pi/a$), where the neighboring Fe atoms are antiparallel to each other. This behavior can be qualitatively explained by noting that the magnetizing effect of the Fe atoms on the nearby Pt atoms decreases as the angle between the Fe moments increases, since their contributions tend to cancel out. Interestingly, the DFT calculations predict that the Pt spin polarizations also form a spiral state, in which the angles between neighboring Pt moments are close to, but not exactly equal to qa. This indicates that a translation by a lattice constant a in real space, combined with a rotation by an angle qa in spin space, remains an approximate local symmetry despite the presence of SO interactions. Nevertheless, the effects of SO coupling and the anisotropy it introduces are not negligible. For example, for $qa = \pi/4$, $\pi/2$, and $2\pi/3$, the angles between neighboring $\boldsymbol{\mu}_{\mathrm{Pt}}$ deviate from the corresponding perfect-spiral values by approximately 2–3°, 3–10°, and 2–8°, respectively. Furthermore, except in the FM state, a misalignment is observed between the Pt and Fe moments, with the Pt moments tending to adopt a direction that lies between those of the noncollinear neighboring Fe moments ($q \neq 0$). Finally, in the AF configuration one finds a very small, site-independent component of μ_{Pt} along the easy y axis, and an alternating, even smaller component along the stripe direction (x axis).

A significant dependence of $\varepsilon_{yx}(q)$ on chirality is induced by applying an EF along the y direction. This is quantified by $\Delta\varepsilon_{\mathrm{DM}}(q) = \varepsilon^{+}_{yx}(q) - \varepsilon^{-}_{yx}(q)$, as shown in Fig. 2(c) for $E_y = 0.5$ V/Å. The large values of $\Delta\varepsilon_{\mathrm{DM}}$ for the $q \simeq \pi/2a$ already indicate that the EF-induced DM couplings between first-NN Fe atoms are particularly important [see Eq. (7)]. In fact, a detailed real-space understanding of the magnetic-order stability in PtFePt stripes can be obtained by calculating the effective interactions between the local Fe moments. To this end, we have fitted the first-principles results for $\varepsilon_{\gamma\delta}(q)$ using the classical spin model introduced in Sec. II A. In doing so, a compromise needs to be reached between identifying the physical relevant interaction range in real space and reducing the residual fitting error by simply increasing the number of model parameters. This balance is particularly important in the present case, where the DFT data are not only limited in number, but also subject to some uncertainties stemming from the subtlety of the SOC effects in the presence of an external EF and from the small total-energy differences involved. In order to identify the physically relevant anisotropies and interaction range, we applied the Akaike information criterion [84,85]. As shown in the Appendix, our analysis indicates that PtFePt and PtMnPt stripes are best described by including first- and second-NN exchange interactions and their anisotropies. A dominant role of first- and second-NN exchange couplings has also been observed in scalar-relativistic calculations of the magnon dispersion relations of pure Fe chains [97].

The calculated magnetic interactions in PtFePt stripes are given in Table I. One observes that the NN isotropic exchange coupling J_{01} is ferromagnetic ($J_{01} > 0$) and that it represents the dominant energy scale. The second NN isotropic coupling J_{02} is also FM, yet an order of magnitude smaller than J_{01}. The orientation-dependent changes in the symmetric NN couplings ΔJ^{γ}_{01} and the local magnetic anisotropies K^{γ} are even smaller, of the order a few meVs. The strongest anisotropies of the symmetric exchange interactions are found within the stripe plane, between the x and y directions. Magnetic anisotropy energies of the same order of magnitude have been found in other one-dimensional TM systems [16].

An interesting consequence of the anisotropies ΔJ^{γ}_{ij} and K^{γ} is the appearance of small discontinuities in the dispersion

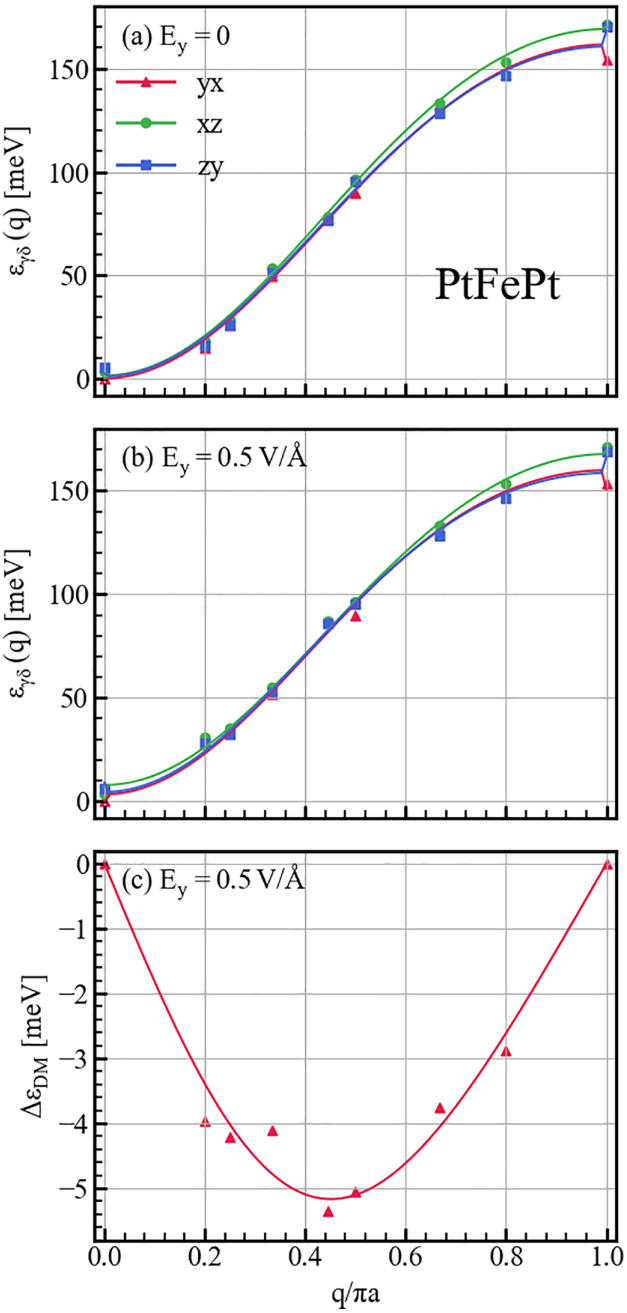


FIG. 2. Dispersion relations of spiral spin-density waves in one-dimensional PtFePt stripes: (a) $\varepsilon_{\gamma\delta}(q) = \mathcal{E}_{\gamma\delta}(q) - \mathcal{E}_0(0)$ in the absence of an external electric field ($\vec{E} = 0$) for different spin-polarization planes $\gamma\delta$. The first letter of the label $\gamma\delta = yx$, xz, and zy indicates the direction of the Fe moments in the collinear $q = 0$ and $q = \pi/a$ configurations. (b) Same as in (a), but for an applied field $E_y = 0.5$ V/Å along the y axis. Note that in (a) ε_{xy} is independent of chirality and in (b) the average over opposite chiralities is shown (see Fig. 1). (c) Chirality of the dispersion relation $\Delta\varepsilon_{\rm DM}(q) = \varepsilon^+_{yx}(q) - \varepsilon^-_{yx}(q)$ for the yx spin-polarization plane when $E_y = 0.5$ V/Å. Because of symmetry, $\varepsilon_{\gamma\delta}$ is independent of chirality in the absence of an external electric field, as well as for the xz and zy planes when $\vec{E} \parallel \hat{y}$. The points are obtained by applying density-functional theory, while the curves show the fits to the first-principles results using the classical spin model described in Sec. II A. The corresponding effective interactions between the Fe moments are listed in Table I.

relations at the zone boundaries $q = 0$ and $q = \pi/a$ for all spin polarization planes $\gamma\delta$ [see Figs. 2(a) and 2(b)]. For any noncollinear spin spiral within the $\gamma\delta$ plane ($q \neq 0, \pi/a$) the local and pairwise anisotropic energy contributions amount to averaging K^γ and K^δ, as well as $\Delta J^\gamma_{0\nu}$ and $\Delta J^\delta_{0\nu}$. This corresponds to the spatial average of $\sin^2(qal)$, $\cos^2(qal)$, $\sin(qal)\sin[qa(l+\nu)]$, and $\cos(qal)\cos[qa(l+\nu)]$ over $0 \leqslant l \leqslant N-1$. For example, in the limit $q \to 0$, we have $\varepsilon_{\gamma\delta}(q \to 0) = (K^\gamma + K^\delta - 2J_{01} - \Delta J^\gamma_{01} - \Delta J^\delta_{01})/2$. In contrast, for the collinear arrangements along a specific direction γ, only the anisotropy terms K^γ and $\Delta J^\gamma_{0\nu}$ contribute. For example, $\varepsilon_{\gamma\delta}(0) = K^\gamma - J_{01} - \Delta J^\gamma_{01}$. As a result, discontinuities arise in the $\varepsilon_{\gamma\delta}(q)$ at the zone boundaries whenever $K^\gamma \neq K^\delta$ or $\Delta J^\gamma_{0\nu} \neq \Delta J^\delta_{0\nu}$. This effect, clearly visible in the DFT calculations, is correctly reproduced by the generalized spin model with the interaction parameters reported in Table I [see Figs. 2(a) and 2(b)]. An analogous behavior is also observed in PtMnPt stripes.

The presence of an external electric field $E_y = 0.5$ V/Å introduces modifications of the symmetric couplings, which in some cases alter the sign of the anisotropies. However, they do not affect the general trends. The most important effect of an external EF is the development of significant DM interactions between first and second NNs. The corresponding DM vectors point along the z direction with $D^z_{01} = -2.5$ meV and $D^z_{02} = -0.2$ meV. Thus, both of these couplings stabilize SDWs within the xy plane with the same chirality $\alpha = -1$. The orientation of the DM vector $\boldsymbol{D}_{ij}$ can be inferred by applying the symmetry rules formulated by Moriya [33]. In the present case, the external electric field $\boldsymbol{E} = (0, E_y, 0)$ points along the y axis, which is perpendicular to the vectors $\boldsymbol{r}_{01}$ and $\boldsymbol{r}_{02}$ connecting first and second NNs along the x axis (see Fig. 1). Taking into account the pseudovector character of $\boldsymbol{D}_{ij}$ and the invariance of the energy upon symmetry transformations, it is easy to see that a reflection across the xy plane leaves both $\boldsymbol{r}_{ij}$ and $\boldsymbol{E}$ unchanged, while reversing the x and y components of $\boldsymbol{D}_{01}$ and $\boldsymbol{D}_{02}$. Consequently, $D^x_{ij} = D^y_{ij} = 0$ for all E_y. Moreover, a reflection across the zx plane reverses both E_y and D^z_{ij}. Therefore, D^z_{ij} is an odd function of E_y, i.e., $D^z_{ij}(-E_y) = -D^z_{ij}(E_y)$.

The EF-induced DM coupling D^z_{01} between NN Fe atoms in PtFePt has been calculated as a function of the field strength E_y. Figure 3 shows that D^z_{01} decreases linearly with increasing E_y, being negative for $E_y > 0$ [$D^z_{ij}(-E_y) = -D^z_{ij}(E_y)$]. Significant cubic corrections cannot be discerned at the considered field strengths ($E_y \leqslant 0.5$ V/Å). The proportionality between D^z_{01} and E_y in the small-field limit indicates the presence of nonvanishing permanent dipole moments $\boldsymbol{p}^+_0$ and $\boldsymbol{p}^-_0$ in the field-free spiral states ($E_y = 0$), whose y components depend on the chirality of the SDW. For PtFePt stripes without any applied field ($E_y = 0$) we obtain $p^+_{0y} = -p^-_{0y} = 0.020$ eÅ for the $q = \pi/2a$ spin spiral. This implies that the EF-induced DM interactions are not simply a consequence of breaking the inversion symmetry of the lattice, for example, through field-induced modifications of the electronic structure or induced dipole moments. Instead, the microscopic origin of the DM coupling lies inherently within the field-free stripes. It stems from the noncollinearity of the SDW and from the specific dependence of SO interactions on the chirality of the magnetic configurations. This chiral effect is only revealed by

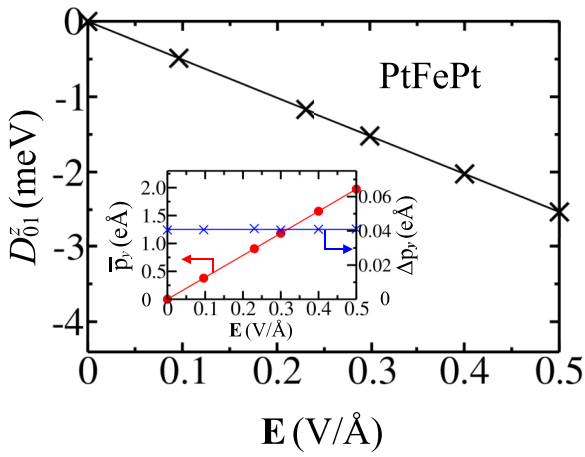


FIG. 3. Dzyaloshinskii-Moriya vector $\boldsymbol{D}_{01} = (0, 0, D^z_{01})$ between nearest-neighbor Fe atoms in PtFePt stripes as a function of the applied electric field $\boldsymbol{E} = (0, E_y, 0)$. The inset shows the corresponding electric dipole moments per unit cell p^α_y along the field for the spin spirals with wave number $q = \pi/2a$ and chirality α: average $\overline{p}_y = (p^+_y + p^-_y)/2$ (left scale) and chiral difference $\Delta p_y = p^+_y - p^-_y$ (right scale).

the electrostatic interaction $-\boldsymbol{p}\cdot\boldsymbol{E}$ between the external EF and the permanent dipole moments $\boldsymbol{p}^+_0$ or $\boldsymbol{p}^-_0$, thus resulting in the antisymmetry of the magnetic couplings. The same qualitative behavior has been found in TM dimers, consistent with the predictions of the spin-current model [31,40]. Quantitatively, previous calculations on $3d$-TM dimers show that the SO-induced permanent dipole moments are an order of magnitude smaller than in PtFePt stripes. For example, in the most favorable case, where the angle θ between NN moments is $\pi/2$, one obtains $p^+_{0y} = -p^-_{0y} \simeq 0.001$ eÅ for the Fe dimer and $p^+_{0y} = -p^-_{0y} \simeq 0.002$ eÅ for the Mn dimer. At least two factors contribute to this trend: the presence of Pt atoms in the stripes, which enhances SO effects, and the discreteness of the energy spectrum in the dimers, which renders SO coupling less efficient.

The zero-field dipole moments depend on the degree of noncollinearity of the magnetic configuration and therefore on the wave number q, vanishing for the collinear FM and AF states. In fact, for not too large fields ($E_y \leqslant 0.5$ V/Å) the chirality of the dispersion relation $\Delta\varepsilon_{\rm DM}(q) = \varepsilon^+_{xy}(q) - \varepsilon^-_{xy}(q)$ is very closely given by $\Delta\varepsilon_{\rm DM}(q) \simeq [p^-_{0y}(q) - p^+_{0y}(q)]E_y = 2p^-_{0y}(q)E_y$, where we have used that $p^+_{0y}(q) = -p^-_{0y}(q)$ owing to the xz-reflection symmetry of the stripe (see next paragraph). Incidentally, one should also note that the electric dipole moments induced by applying an EF perpendicular to the stripes are not at all negligible. They increase almost linearly with E_y, rapidly becoming much larger than the permanent moments, which stem from SO interactions. This is demonstrated in the inset of Fig. 3, where both the average induced electric dipole moment $\overline{p}_y = (p^+_y + p^-_y)/2$ and the chiral difference $\Delta p_y = p^+_y - p^-_y$ are shown as a function of the applied EF for the $q = \pi/2a$ spin spiral. However, the linear electric polarizability, despite being dominant, is independent of chirality. Therefore, it does not contribute to the DM couplings, in agreement with the known odd parity of D^z_{ij} with respect to E_y. Only the much weaker second-order contribution to the induced dipole moments gives rise to a small cubic correction to $D^z_{ij}(E_y)$. The same qualitative behavior applies to two-dimensional layered structures [42].

The orientations of the permanent dipole moments $\boldsymbol{p}^+_0$ and $\boldsymbol{p}^-_0$ are closely linked to the symmetry of the noncollinear magnetic configurations with respect to the lattice structure of the stripes. Let us recall that the electronic density $n(r)$ is invariant upon time inversion and therefore the electric dipole moments are invariant upon reversing all local magnetic $\boldsymbol{\mu}_i$. Moreover, concerning spatial symmetry operations, $\boldsymbol{p}_0$ transforms as a vector whereas $\boldsymbol{\mu}_i$ as a pseudovector. Consider a $q = \pi/2a$ spiral in the absence of an external EF with spin polarizations within the xy plane and a given chirality $+$ or $-$. Applying a time-inversion operation followed by a reflection across the xy plane does not change the magnetic configuration but reverses the z component of any dipole moment $\boldsymbol{p}_0$. Consequently, $p^+_{0,z} = p^-_{0,z} = 0$. Applying now a reflection across the zx plane, reverses one of every two local moments $\boldsymbol{\mu}_i$ (those pointing along the x direction) while leaving the others unchanged (those pointing along the y direction). This amounts to a change in the chirality of the SDW. Concerning the electric dipoles, the zx reflection changes the sign $p_{0,y}$ while leaving $p_{0,x}$ and $p_{0,z}$ unchanged. Consequently, $p^+_{0,y} = -p^-_{0,y}$, $p^+_{0,x} = p^-_{0,x}$, and $p^+_{0,z} = p^-_{0,z}$. The chirality of the permanent dipole moment, which defines the dominant linear contribution to the EF-induced DM interactions, is given by $\Delta\boldsymbol{p}_0 = \boldsymbol{p}^+_0 - \boldsymbol{p}^+_0 = (0, 2p^+_{0,y}, 0)$. In other words, the EF-induced $\boldsymbol{D}_{ij}$ arises from the chirality of the dipole moment along the direction $\boldsymbol{r}_{ij} \times (\boldsymbol{\mu}_i \times \boldsymbol{\mu}_j)$, which lies within the plane spanned by $\boldsymbol{\mu}_i$ and $\boldsymbol{\mu}_j$, and is perpendicular to the vector connecting the Fe atoms. This is consistent with the electric polarization derived from the spin current [40,41,98].

B. PtMnPt stripes

In Fig. 4, the frozen-magnon dispersion relations $\varepsilon_{\gamma\delta}(q)$ of PtMnPt stripes are shown. As in Fig. 2, the discrete points are obtained from supercell DFT calculations, whereas the curves correspond to the fits of the first-principles results using the classical spin model of Sec. II A. The effective magnetic interactions derived from the fits are reported in Table I. First of all, one observes a strong stability of the antiferromagnetic order for all spin-polarization planes. This behavior is primarily driven by the symmetric exchange couplings between first NNs, as evidenced by the approximate $\cos(qa)$ dependence of $\varepsilon^\alpha_{\gamma\delta}(q)$. These main trends are not altered by applying an external electric field $E_y = 0.5$ V/Å [cf. Figs. 4(a) and 4(b)]. The results for different magnetization directions and spin-polarization planes reveal significant anisotropies in the total energy and in the underlying exchange interactions. In particular, we obtain that the most stable spin configuration consists of alternating Mn moments pointing along the stripe direction (x axis). The MAE associated to a uniform rotation of the stable AF order along the x axis toward the y and z directions are $\Delta\mathcal{E}_{xy} = -9.7$ meV (-10.4 meV) and $\Delta\mathcal{E}_{xz} = -19.0$ meV (-19.8 meV) for an external EF $E_y = 0.5$ V/Å ($E_y = 0$). The stability of the x-axis magnetization is mainly the consequence of the anisotropy of the NN symmetric interactions. In fact, the results for ΔJ^γ_{01} given in Table I show that

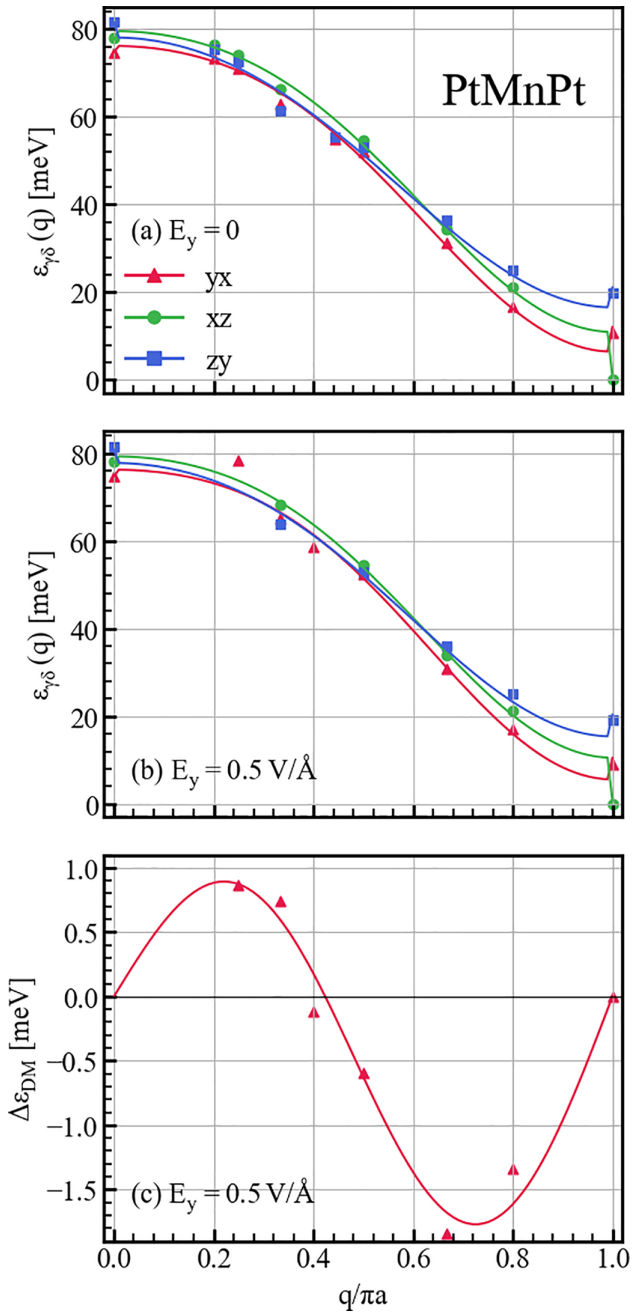


FIG. 4. Dispersion relations of spiral spin-density waves in one-dimensional PtMnPt stripes. (a) $\varepsilon_{\gamma\delta}(q) = \mathcal{E}_{\gamma\delta}(q) - \mathcal{E}_0(0)$ in the absence of an external electric field ($\vec{E} = 0$) for different spin-polarization planes $\gamma\delta$. The first letter of the label $\gamma\delta = yx$, xz, and zy indicates the direction of the Mn moments in the collinear $q = 0$ and $q = \pi/a$ configurations. (b) Same as in (a), but for an applied field $E_y = 0.5$ V/Å along the y axis. Note that in (a) ε_{xy} is independent of chirality and in (b) the average over opposite chiralities is shown (see Fig. 1). (c) Chirality of the dispersion relation $\Delta\varepsilon_{\rm DM}(q) = \varepsilon^{+}_{yx}(q) - \varepsilon^{-}_{yx}(q)$ for the yx spin-polarization plane when $E_y = 0.5$ V/Å. Because of symmetry, $\varepsilon_{\gamma\delta}$ is independent of chirality in the absence of an external electric field, as well as for the xz and zy planes when $\vec{E} \parallel \hat{y}$. The points are obtained by applying density-functional theory, while the curves show the fits to the first-principles results using the classical spin model described in Sec. II A. The corresponding effective interactions between the Mn moments are listed in Table I.

the NN exchange couplings for moments along the x direction are approximately 5 meV stronger than the isotropic coupling $J_{01} \simeq 33$ meV, whereas the couplings along the y and z directions are weaker by about 2–3 meV. The local anisotropy contributions K^{γ} are not decisive in this case. Although they clearly favor an orientation of the local magnetic moments within the xy plane, they do not strongly distinguish between the x and y directions, showing only a slight preference for the latter (see Table I). Notice, moreover, the presence of small discontinuities in $\varepsilon^{\alpha}_{\gamma\delta}(q)$ at the zone boundaries. As already discussed in the case of PtFePt stripes, these arise from the anisotropy of symmetric exchange couplings ΔJ^{γ}_{01} and local energy contributions K^{γ}.

The local magnetic moments at the Mn atoms, calculated within the Wigner-Seitz spheres, are close to full saturation, taking almost the same value $\mu_{\rm Mn} \simeq 4.22\,\mu_B$ for all q and spin-polarization planes. As in the case of Fe, the Mn moments are found to be strongly stable, which supports the validity of the spin-model approach. The Pt moments vanish almost completely in the AF ground state ($q = \pi/a$). They increase with decreasing q, reaching a maximum value of $\mu_{\rm Pt} \simeq 0.2\,\mu_B$ around $q \simeq \pi/3$, and then decrease slowly as q approaches the FM configuration, where $\mu_{\rm Pt}$ lies in the range 0.12–0.17 μ_B, depending on the orientation of the Mn moments. The local magnetic moments are only marginally affected by the application of an external electric field ($E_y \leqslant 0.5$ V/Å).

The frozen-magnon dispersion relations can be interpreted from a local perspective by considering the effective magnetic interactions between the Mn moments, which are given in Table I. One observes that the isotropic symmetric exchange coupling J_{01} defines the largest energy scale, being an order of magnitude stronger than the second-neighbor coupling J_{02}. The anisotropies ΔJ^{γ}_{01} of the symmetric NN couplings are of the order of a few meV. Although quantitatively significant in absolute terms, their relative importance is rather limited in the case of first neighbors, since ΔJ^{γ}_{01} amounts to about 5–15% of J_{01} (see Table I). The local contributions K^{γ} to the magnetic anisotropy clearly stabilize the orientation of the magnetic moments within the xy plane containing the stripe, but they are very small between the x and y directions. As already discussed, the easy direction of the magnetic moments in the ground-state AF configuration is defined by the largest symmetric exchange coupling, which corresponds to the x axis. Notice that whenever the relative stability stems from interactions, it depends on q. Therefore, as expected, in the FM configuration ($q = 0$) the easy magnetization direction changes to the y axis, where the positive J_{01}, unfavorable for parallel moments, is weaker.

Applying an external electric field $E_y = 0.5$ V/Å causes minor changes in the symmetric exchange couplings and local anisotropies, except for K^x and K^y. In particular, the signs of ΔJ_{0v} and K^{γ} remain the same. The central consequence of applying an EF is the development of significant DM interactions between first and second neighbors. According to symmetry, the DM vectors point along the z direction [33], thereby stabilizing SDWs within the xy plane. These are the same symmetry rules that apply to PtFePt stripes. However, in contrast to the Fe case, in PtMnPt stripes the chirality of the dispersion relation of xy spirals, $\Delta\varepsilon_{\rm DM}(q) = \varepsilon^{+}_{yx}(q) - \varepsilon^{-}_{yx}(q)$,

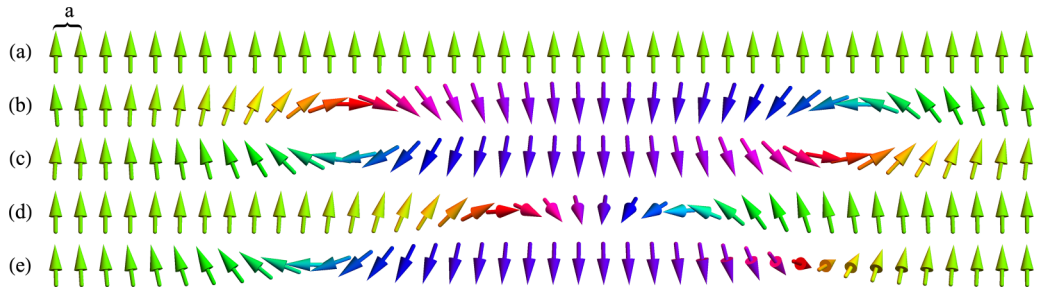


FIG. 5. Low-energy metastable configurations and transition states in an PtFePt stripe subjected to an external electric field $E = 0.5$ V/Å. (a) Single-domain ferromagnetic ground state with all local moments aligned along the y axis. (b) Two-domain excited state with winding number $\eta_z = 1$, each Néel domain wall having $\eta_z = 1/2$. (c) Two-domain excited state with $\eta_z = -1$, each Néel domain wall having $\eta_z = -1/2$. (d) Transition state between the FM ground state (a) and the two-domain excited state (b). (e) Transition state between the FM ground state (a) and the two-domain excited state (c). The arrows show the orientation of $\hat{\mu}_i$ in 3D and the colors represent the projection of $\hat{\mu}_i$ within the xy plane. The supercell comprises $N = 40$ PtFePt units. It is chosen to be compact while still fully capturing the domain-wall profile.

changes sign as a function of q. As shown in Fig. 4(c), $\Delta\varepsilon_{\mathrm{DM}} > 0$ for $q < 0.4\pi/a$, stabilizing a clockwise $(-)$ SDW, whereas $\Delta\varepsilon_{\mathrm{DM}} < 0$ for $q \geqslant \pi/2a$, stabilizing a counterclockwise $(+)$ SDW. In the intermediate range ($q \simeq 0.4\pi/a$) both chiralities are nearly degenerate. From a local perspective, this behavior reflects that the second neighbor $D^z_{02} = 0.6$ meV has the opposite sign as the first neighbor $D^z_{01} = -0.3$ meV and is stronger in absolute value (see Table I). Although the EF-induced DM interactions in Mn stripes are an order of magnitude smaller than in Fe stripes, the competition between first- and second-neighbor couplings renders them particularly interesting.

IV. METASTABLE STATES AND ELEMENTARY TRANSITIONS

In the following, the classical Heisenberg model derived in the previous section is employed to investigate the energy landscapes of PtFePt and PtMnPt stripes. To this end, the low-lying metastable states and the elementary transitions between them are determined by considering supercells containing up to $N = 200$ PtFePt or PtMnPt units.

A. PtFePt stripes

We begin by analyzing the magnetic configurations of PtFePt stripes subjected to an external electric field $E_y = 0.5$ V/Å. As previously discussed, the ground state is FM, with the Fe moments aligned along the y axis (see also Sec. III A). Ferromagnetic states with other magnetization directions are unstable; they do not correspond to local minima of the energy landscape. The metastable excited configurations consist in introducing magnetic domains (MDs) to the FM ground state. Figure 5 depicts the lowest-energy configurations including the FM ground state (a) and the metastable excited states (b) and (c) comprising two MDs separated by Néel-type domain walls (DWs) in which the magnetic moments rotate within the xy plane. Notice that the sense of rotation of the local moments is the same in both DWs of a given configuration: anticlockwise in (b) and clockwise in (c), as we move from left to right. No metastable states have been found, in which the delimiting DWs have opposite chiralities. In fact, starting from such a configuration and following the energy gradient, one finds that the DWs with opposite chiralities annihilate each other without encountering an energy barrier.

To characterize the metastable configurations and their DWs in more detail, we introduce the winding number η_z, which represents the cumulative angle covered by the rotating magnetization density around the z axis measured in numbers of full turns. This is given by

$$\eta_z = \frac{1}{2\pi}\sum_{m=1}^{N} \mathrm{atan2}[(\hat{\boldsymbol{\mu}}_i \times \hat{\boldsymbol{\mu}}_{i+1}) \cdot \hat{\boldsymbol{e}}_z,\ \hat{\boldsymbol{\mu}}_i \cdot \hat{\boldsymbol{\mu}}_{i+1}], \tag{10}$$

where the summand gives the angle between the local moments as we turn $\boldsymbol{\mu}_i$ toward $\boldsymbol{\mu}_{i+1}$, with positive (negative) sign for a counterclockwise (clockwise) sense of rotation, and N is the number of local moments in the considered configuration (for example, a single DW or a state with multiple MDs). Thus, a clockwise π rotation of the magnetic moments within the xy plane yields $\eta_z = -1/2$, whereas an anticlockwise π rotation corresponds to $\eta_z = 1/2$. The winding numbers of the configurations shown in Figs. 5(a)–5(c) are $\eta_z = 0$, 1, and -1, respectively. In terms of η_z, the magnetic configurations shown in Figs. 5(b) and 5(c) owe their local stability to having η_z different from that of the FM ground state. Consequently, these configurations cannot evolve spontaneously into the ground state. In contrast, two-MD configurations delimited by DWs with opposite chiralities ($\eta_z = \pm 1/2$) share the same winding number as the ground state and are therefore unstable, as they can relax spontaneously to it. The fact that the presence of a stabilizing energy barrier involves a discrete change in η_z reflects a form of topological protection, also observed in other systems, such as skyrmion-hosting thin films [99,100].

The higher-energy metastable states of the stripes correspond to creating further magnetic domains. Notice that in our calculations only an even number $2m$ ($m \in \mathbb{N}$) of MDs and DWs are compatible with the assumed periodic boundary conditions. Furthermore, since all DWs must have the same chirality to ensure metastability, the winding numbers of the metastable states are integers $\eta_z = \pm m$. The only LM with $\eta_z = 0$ is the FM ground state. Notably, after thorough search,

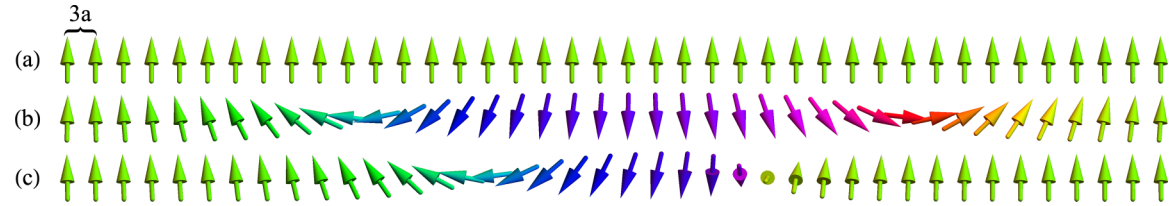


FIG. 6. Low-energy metastable configurations and transition states in a PtFePt stripe in the absence of external electric fields. (a) Single-domain ferromagnetic (FM) ground state with all local moments aligned along the y axis. (b) Two-domain excited state with winding number $\eta_z = 1$, where each Néel domain wall has $\eta_z = 1/2$. (c) Transition state between the FM ground state (a) and the two-domain excited state (b). The arrows show the orientation of $\hat{\mu}_i$ in 3D and the colors represent the projection of $\hat{\mu}_i$ within the xy plane. A supercell containing $N = 120$ PtFePt units is used. It is chosen to be compact while still fully capturing the domain wall profile. For the sake of clarity and compactness, the configurations are coarse grained by averaging the orientations within groups of three neighboring local moments.

no metastable configurations have been found that deviate from this pattern. In other words, all observed metastable states share the same underlying magnetic texture characterized by domain magnetizations strictly aligned along the y axis and DWs confined to the xy plane. From the perspective of magnetic interactions, this is mainly a consequence of the local anisotropy energies K^γ, which favor a magnetization along the y axis, and the anisotropic NN exchange couplings, which are strongest along the x axis (see Sec. III A). As discussed below, the antisymmetric DM couplings are not essential for the topological protection or for defining the spin-polarization plane of the DWs. They are, however, central to the relative stability of DWs with opposite chiralities.

The metastable magnetic configurations for $E_y = 0$ are qualitatively similar to those found for $E_y = 0.5$ V/Å. The ground state is a FM state with magnetization along the y axis. The metastable excited configurations are obtained by introducing MDs with reversed magnetization along the easy y axis. The same constraints apply, namely, that the total number of MDs and DWs must be even, as required by the periodic boundary conditions, and that all the DWs must have the same chirality to ensure topological protection. In Fig. 6, the ground state (a) and first-excited metastable state (b) are shown at zero field. The latter comprises two magnetic domains separated by Néel-type DWs in which the local moments rotate in anticlockwise sense. The mirror-symmetric state with clockwise DWs is also metastable and by all means equivalent to the one shown in Fig. 6(b). Let us recall that in the absence of an EF the stripes are invariant upon inversion and therefore the DM interactions vanish.

The most notable difference between the $E_y = 0$ and $E_y = 0.5$ V/Å results is the DW width, which is substantially reduced in the presence of the EF. To clarify the origin of this change of behavior and to correlate it with the field-induced changes in the effective magnetic interactions, we estimate the DW width L_{DW} by taking into account the anisotropy of all the model parameters: symmetric exchange J^γ_{0v}, local energy K^γ, and antisymmetric DM coupling D^z_{0v}. Assuming a uniform rotation of the local magnetic moments along a DW in a FM or AF stripe, one obtains

$$L_{DW} = \frac{\pi a}{\sqrt{2}} \sqrt{\frac{|J^e_{01}| + |J^h_{01}| + 8J_{02}}{|J^e_{01}| - |J^h_{01}| + K^h - K^e}}, \tag{11}$$

where e and h denote the easy and hard axis, respectively. Substituting the calculated PtFePt parameters from Table I with $e = y$ and $h = x$ yields $L_{DW}/a \simeq 12$ for $E_y = 0.5$ V/Å and $L_{DW}/a \simeq 41$ for $E = 0$, in very good agreement with the unconstrained numerical minimizations.

The reduction in DW length under the applied EF can then be traced to significant changes in the symmetric-exchange anisotropies $\Delta J_1 = J^y_{01} - J^x_{01}$ ($\Delta J_2 = J^y_{02} - J^x_{02}$), from 8.1 meV (−1 meV) for $E_y = 0$ to 5.8 meV (−5.6 meV) for $E_y = 0.5$ V/Å. As a result, the total anisotropy energy $\Delta E = \Delta J_1 + \Delta J_2 + K^x - K^y$ increases substantially from 0.6 meV to 8.3 meV, which qualitatively explains the reduction of L_{DW} by more than a factor three. By contrast, the EF-induced changes in the average exchange couplings, about 4–6%, are not so important in this context (see Table I). Finally, notice that the DM interactions do not affect L_{DW}, since their contribution to the DW energy, approximately equal to $\alpha\pi(D^z_{01} + 2D^z_{02})$, depends on the DW chirality $\alpha = \pm 1$ but not on the wall width.

A more detailed understanding of the magnetic behavior of PtFePt stripes can be gained by exploring the underlying energy landscape as a function of the orientations $\hat{\boldsymbol{\mu}}_i$ of the local Fe moments. Figure 7 shows the energy profiles along the minimum energy paths connecting the FM ground state with the two-domain excited states having winding numbers $\eta_z = \pm 1$, for $E_y = 0$ and $E_y = 0.5$ V/Å. The stability of the FM ground state is remarkable. As the field $E_y = 0.5$ V/Å is applied, the already important uphill energy barrier $\Delta\varepsilon = 68$ meV for $E_y = 0$ rises to $\Delta\varepsilon = 150$ meV for the favorable chirality ($\eta_z > 0$) and even to $\Delta\varepsilon = 175$ meV for the unfavorable one ($\eta_z < 0$).

Let us recall that in the absence of an EF the energy of any spin configuration and its mirror image are the same, a direct consequence of inversion symmetry and the absence of DM interactions. Putting aside the translational symmetry along the stripe, each metastable state is two-fold degenerate for $E_y = 0$. This degeneracy is lifted when an EF is applied, as it introduces DM interactions between the local moments.

The substantial energy differences between the metastable two-domain states for $E_y = 0$ and $E_y = 0.5$ V/Å is particularly noteworthy, given the qualitative similarities between their magnetic configurations. The largest part of the change in the excitation energies upon applying an electric field is unrelated to the DM couplings. Indeed, when the DM interaction is neglected, the change in the excitation energy upon applying the EF amounts to $\Delta\varepsilon = 109$ meV. From an electronic point of view this difference stems from the fact that spin spirals with small wave vectors q are energetically less

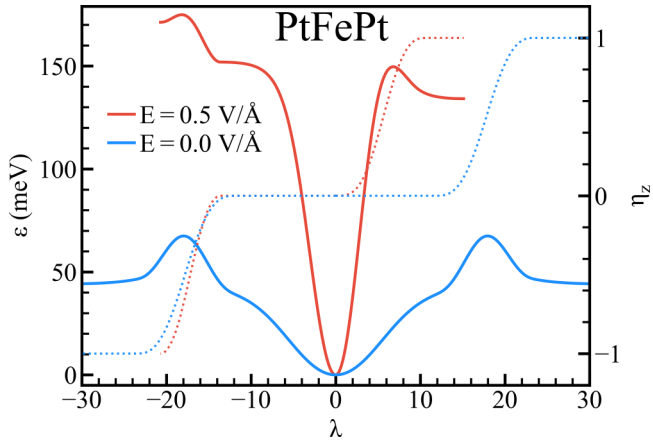


FIG. 7. Energy profile along the minimum-energy path connecting the single-domain FM ground state with the two-domain excited states with winding numbers $\eta_z = 1$ ($\lambda > 0$) and $\eta_z = -1$ ($\lambda < 0$). Results are shown for $E_y = 0$ (blue solid curve) and $E_y = 0.5$ V/Å (red solid curve) as functions of the path coordinate λ for a PtFePt stripe having $N = 200$ PtFePt units and periodic boundary conditions (left-hand-side energy scale). The corresponding winding numbers η_z along the reaction path are given by the dotted curves (right-hand-side scale). Positive (negative) λ corresponds to positive (negative) η_z.

favorable in the presence of an EF [cf. Figs. 2(a) and 2(b)]. This trend is also evident in the parameters of the Heisenberg model (Table I). After applying the EF, J_1^x decreases by 3.6 meV, while J_2^y increases by 4.1 meV. This change effectively increases the energy cost of forming spiral configurations since it implies rotating the magnetic moments away from the y axis toward the x axis. The remaining chiral difference (± 16.5 meV) is the consequence of DM interactions, which can be approximated by $2\pi(D_{01}^z + D_{02}^z) = 17$ meV.

The downhill barriers as we go from the two-domain states toward the FM ground state are comparatively small. For $E_y = 0$ we have $\Delta\varepsilon = 24$ meV and for $E_y = 0.5$ V/Å we find $\Delta\varepsilon = 16$ meV for the $\eta_z = 1$ state or $\Delta\varepsilon = 4$ meV for the $\eta_z = -1$ state. Such small values of the energy barriers are inconsistent with an annihilation of DWs in which the local moments remain confined to the xy plane. In fact, any DW annihilation process restricted to the xy plane would necessarily involve a configuration with antiparallel spins at adjacent sites, resulting in significantly higher energy barriers, of the order of the symmetric exchange interactions. Along the actual MEP, the system circumvents such unfavorable configurations by rotating the local moments out of the xy plane. By exploiting the third spatial dimension, a continuous transition path with much lower barriers becomes possible, as it relies primarily on the local and exchange anisotropies, which are at least an order of magnitude weaker than the exchange couplings (see Table I). This mechanism, often referred to as escape through the third dimension, has been observed in a range of low-dimensional magnetic systems, especially in the presence of magnetic fields [101]. Moreover, the energy barriers responsible for the topological protection of the metastable states are given by the local anisotropy energies and the anisotropy of the symmetric exchange couplings rather than by DM couplings. This is the main reason for the stability of the metastable state with unfavorable chirality for $E_y = 0.5$ V/Å.

The transition states between the FM ground state and two-domain configurations are depicted in Figs. 5(d) and 5(e) for $E_y = 0.5$ V/Å and in Fig. 6(c) for $E_y = 0$. Consider, for instance, Fig. 5(d), which corresponds to the transition with $\eta_z > 0$. In the TS, the two DWs are found to be very close to each other, and the MD with reversed magnetization along the y axis has practically disappeared [see violet arrow in Fig. 5(d)]. Near these merging DWs, the local moments are rotated out of the xy plane towards the positive z axis by rotating the left part clockwise and the right part anticlockwise around the x axis, for which the DM interactions are zero. The result is a configuration consisting of two DW-like spin arrangements with opposite chiralities. The DWs can then annihilate each other, leading to a downhill evolution toward the FM state. An analogous transition mechanism is found for $E_y = 0$ [see Fig. 6(c)].

The relaxation process connecting the two-domain state with the unfavorable chirality ($\eta_z = -1$) and the ground state follows a qualitatively different mechanism as the one where the DM coupling stabilizes the DWs ($\eta_z > 0$). The TS with $\eta_z < 0$ is depicted in Fig. 5(e). In this case, the DWs remain spatially separated and, notably, only one DW (the right one in the present case) exhibits a significant out-of-plane rotation, while the other one remains practically unchanged. The result is a transient configuration in which the chirality of the right DW is reversed. After some further relaxation, this leads to a state with two spatially separated DWs having opposite chiralities and magnetic moments within the xy plane. Note that the winding number changes from $\eta_z = -1$ to the ground-state value $\eta_z = 0$ along the process. Although such a configuration is unstable, the actual annihilation of the DWs can only occur once they are close together. Since the energy of the system is nearly independent of separation when the DWs are far apart, bringing them together proceeds through an almost perfectly flat region of the EL. This behavior manifests as an extended plateau in the energy as a function of the path coordinate λ (see red curve in Fig. 7 for $-15 \leqslant \lambda \leqslant -10$). Furthermore, notice that throughout the process of bringing the DWs together, where ε is nearly constant, as well as in the subsequent annihilation, where ε drops to zero, the winding number remains equal to the ground-state value $\eta_z = 0$ and all $\boldsymbol{\mu}_i$ lie within the xy plane.

Although Fig. 7 shows only the energy profiles between the ground state and the lowest-energy metastable states, it captures all the essential information needed to understand the full energy landscape. Indeed, DWs can be regarded as independent entities, provided that the stripe is sufficiently long. Consequently, the energy of a given metastable state scales linearly with the number of DWs, with a proportionality constant that depends on their chirality. Furthermore, the relaxation mechanisms associated with the annihilation and creation of DWs remain the same, regardless of the number of existing MDs, since each transition proceeds through the same local processes, as previously discussed in the two-domain case. Consequently, the ensemble of metastable states of the infinite stripe consists of two disjoint sets of LM, energetically organized in the form of a stair whose "steps" are by

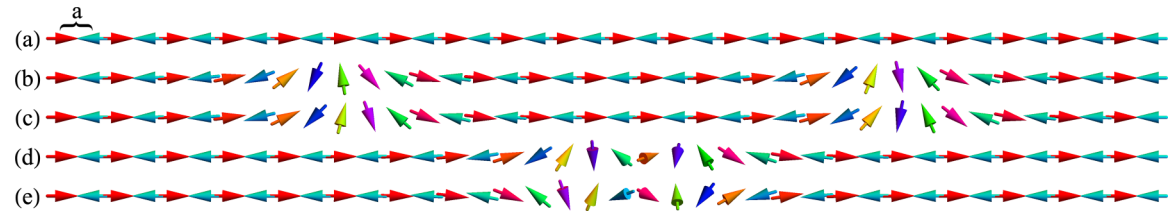


FIG. 8. Low-energy metastable configurations and transition states in PtMnPt stripes subjected to an external electric field $E_y = 0.5$ V/Å. (a) Single-domain antiferromagnetic ground state with all local moments aligned along the x axis. (b) Two-domain metastable excited state with winding number $\eta_z = -1$, each Néel domain wall having $\eta_1 = -1/2$. (c) Two-domain excited state with $\eta_z = 1$, each domain wall having $\eta_z = 1/2$. (d) Transition state between the AF ground state and the two-domain excited state (b). (e) Transition state between the AF ground state and the two-domain excited state (c). The arrows show the orientation of $\hat{\mu}_i$ in 3D and the colors represent the projection of $\hat{\mu}_i$ within the xy plane. A supercell containing $N = 40$ PtFePt units is used, which fully captures the domain-wall profiles, also found in much larger supercells.

all means analogous to the energy profiles shown in Fig. 7. It is important to recall that no true metastable state (i.e., a LM in the EL) can be constructed by considering DWs with different chiralities, even in the absence of DM coupling ($E_y = 0$), as neighboring DWs with opposite chiralities would spontaneously annihilate each other. The MEP connecting two configurations with opposite winding numbers necessarily goes over the FM ground state.

To assess the mobility of DWs in PtFePt stripes, we computed the MEP between a metastable two-domain configuration and the same configuration translated by one lattice spacing. As initial guess for the NEB calculation, we assumed a coherent rotation of the local magnetic moments, which represents the shortest path in the configurational space $S(2)^N$. Even this unrelaxed initial path yields a remarkably small energy barrier of the order of $\Delta\varepsilon = 10^{-2}$ meV. Upon relaxation of the path, the energy barrier further decreases to $\Delta\varepsilon = 10^{-6}$ meV, which is close to the numerical accuracy of our calculations. Within the available numerical precision, it is not possible to rigorously conclude whether a finite barrier is present or whether the translation is genuinely barrierless. Although the distinction is immaterial from a practical point of view, it remains an intriguing theoretical question nonetheless. The transition mechanism closely resembles a coherent rotation. The changes in the angles of the local moments along the optimal path and along the coherent path always differ by less than 1%. These results demonstrate that near the metastable states the energy landscape of perfectly periodic stripes is exceptionally flat with respect to translations, enabling easy displacements of DWs under small currents or magnetic fields. To explore the matter further, we repeated the calculations using a much simpler model, by retaining only first NN isotropic exchange and local anisotropy (i.e., setting $\Delta J_{ij}^{\gamma} = 0$ and $\boldsymbol{D}_{ij} = 0$). The same behavior was observed, indicating that the results are not qualitatively affected by exchange anisotropies or second-neighbor couplings. The high domain-wall mobility is a key feature of magnetic 1D systems, which has been exploited in the context of nanowires and spintronic applications [102,103].

B. PtMnPt stripes

The properties of the PtMnPt stripes are qualitatively different from those of PtFePt. Figure 8 illustrates the magnetic configurations of the ground state, low-energy metastable states, and transition states for a stripe comprising $N = 40$ PtMnPt units in the supercell. As discussed in Sec. III B, the ground state of PtMnPt stripes is antiferromagnetic, with alternating Mn moments aligned along the x axis. Antiferromagnetic configurations with other magnetization directions do not correspond to local minima and are therefore unstable.

The metastable excited configurations correspond to introducing magnetic domains into the AF ground-state background. Figures 8(b) and 8(c) display the two lowest-energy metastable states, each comprising two AF domains separated by Néel-type DWs in which the Mn moments rotate within the xy plane. As in the PtFePt stripes (Sec. IV A) both DWs exhibit the same sense of rotation: clockwise in (b), each wall with winding number $\eta_z = -1/2$, and anticlockwise in (c), each wall with $\eta_z = 1/2$. Configurations in which the DWs have opposite winding numbers are found to be unstable. Higher-energy metastable states can be constructed by introducing additional MDs. The same constraints as in PtFePt stripes apply: The number of MDs and DWs in a metastable configuration is even, equal to $2m$ with $m \in \mathbb{N}$, as required by the periodic boundary conditions, and all DWs share the same chirality, which implies $\eta_z = \pm m$. No other kind of metastable configurations have been identified after thorough exploration.

The metastable configurations for $E_y = 0$ are extremely similar to those found for $E_y = 0.5$ V/Å. Figure 9 shows the low-energy metastable configurations in the absence of an external EF. Besides the AF ground state, one finds excited configurations that include additional MDs. The first-excited metastable state at zero field shown in Fig. 6(b) comprises two AF domains separated by Néel-type DWs, in which the local moments rotate clockwise within the xy plane as we move from left to right. The mirror image of this state, in which the $\boldsymbol{\mu}_i$ rotate in anticlockwise sense is also metastable and has the same energy owing to the inversion symmetry of the Hamiltonian in the absence of external EFs. The differences between the $E_y = 0$ and $E_y = 0.5$ V/Å metastable configurations are so small that they cannot be discerned by visual inspection.

The width of the domain walls in the excited metastable states is not significantly affected by applying an external EF. From the configurations shown in Figs. 5(b), 5(c), and 9(b) one estimates $L_{DW}/a \simeq 7$–8 for both $E_y = 0$ and $E_y = 0.5$ V/Å. This coincides with the result $L_{DW}/a = 8$

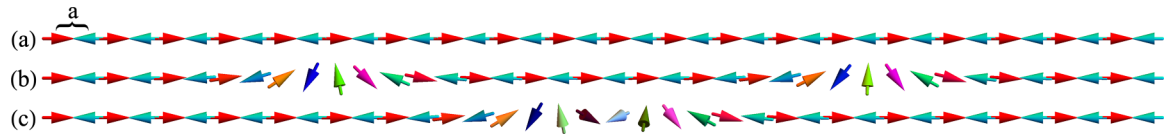


FIG. 9. Low-energy metastable configurations and transition state of a PtMnPt stripe in the absence of external electric fields. (a) Antiferromagnetic ground state with local moments aligned along the x axis, (b) two-domain metastable state with winding number $\eta_z = -1$, and (c) transition state between the FM ground state and the two-domain excited state (b). The mirror images of (b) and (c) are also stationary points and have the same energy. A supercell containing $N = 40$ PtMnPt units is used, which fully captures the domain-wall profiles, also found in much larger supercells.

obtained using Eq. (11) and the interaction parameters listed in Table I. A notable feature of PtMnPt stripes is that the DW width is primarily governed by the anisotropy of the symmetric exchange interactions, since the local anisotropy between the x and y axes is very small: $\Delta K = K_y - K_x = 0.1$ meV for $E_y = 0$ and $E_y = 0.5$ V/Å. Therefore, neglecting the anisotropy of the exchange interactions would result in a serious overestimation of the DW width, failing to capture the actual physical behavior of these systems.

To gain deeper insight into the effects of an external EF on PtMnPt stripes we consider the corresponding energy landscapes. Figure 10 shows the energy profile of the MEPs connecting the AF ground state with the two lowest excited states with winding numbers $\eta_z = \pm 1$, for $E_y = 0$ (blue curve) and $E_y = 0.5$ V/Å (red curve). In both cases, the AF ground state is remarkably stable, separated from its adjacent excited states by substantial energy barriers: $\Delta\varepsilon = 154$ meV for $E_y = 0$ and $\Delta\varepsilon = 146$ meV ($\Delta\varepsilon = 159$ meV) for $E_y = 0.5$ V/Å and $\eta_z = -1$ ($\eta_z = 1$).

In the absence of an external EF, the metastable states with opposite chiralities are degenerate, as required by inversion symmetry. The energy of the first-excited states for $E_y = 0$ is $\varepsilon_1 = 138$ meV. Upon applying an EF this degeneracy is lifted. For $E_y = 0.5$ V/Å, we obtain $\varepsilon_1 = 123$ meV for the $\eta_z = -1$ state and $\varepsilon_1 = 142$ meV for the $\eta_z = 1$ state. The splitting $\Delta\varepsilon_{DM} = \varepsilon_1^+ - \varepsilon_1^- = 19$ meV is considerably smaller than in PtFePt stripes, which is consistent with the weaker DM interactions. The value of $\Delta\varepsilon_{DM}$ can be explained by assuming that the rotation of the local moments within the DWs is uniform and that the DW lengths $L_{DW} \gg a$, although the latter is not quite true in the present case. In this way one obtains the relation $\Delta\varepsilon_{DM} = 4\pi(-D_{01}^z + 2D_{02}^z)$, which yields $\Delta\varepsilon_{DM} \simeq 19$ meV using the values for D_{0v}^z given in Table I. Among the specifics of DM interactions in AF chains it is interesting to note that the first and second nearest-neighbor DM couplings favor the same chirality when they have opposite signs. This is indeed the case for PtMnPt, where $D_{01}^z < 0$ and $D_{02}^z > 0$ both stabilize clockwise DWs. Furthermore, notice that in PtMnPt the DM coupling between second NNs gives a much stronger contribution to the DW energies than the first NN coupling (see Table I). Nevertheless, the difference in energy between the metastable states for $E_y = 0$ and $E_y = 0.5$ V/Å is much less important quantitatively than in PtFePt stripes, highlighting the more subtle influence of EFs in the Mn-based system.

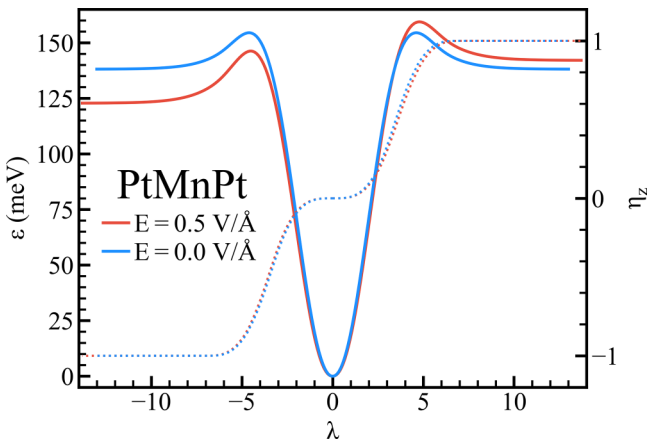


FIG. 10. Energy profile along the minimum energy path connecting the single-domain AF ground state with the two-domain excited states with winding numbers $\eta_z = 1$ ($\lambda > 0$) and $\eta_z = -1$ ($\lambda < 0$). Results are shown for $E_y = 0$ (blue solid curve) and $E_y = 0.5$ V/Å (red solid curve) as functions of the path coordinate λ for a PtMnPt stripe having $N = 200$ PtMnPt units and periodic boundary conditions (left-hand-side energy scale). The corresponding winding numbers η_z along the reaction path are given by the dotted curves (right-hand-side scale). Positive (negative) λ corresponds to positive (negative) η_z.

The downhill energy barriers separating the excited states from the AF ground state are relatively small: $\Delta\varepsilon = 23$ meV for the more stable $\eta_z = -1$ state and $\Delta\varepsilon = 13$ meV for the $\eta_z = 1$ state ($E_y = 0.5$ V/Å). The MEP and intermediate TS associated with DW annihilation and relaxation toward the single-domain ground state are qualitatively very similar to those observed in PtFePt stripes either at $E_y = 0$, as well as in configurations with favorable chirality at $E_y = 0.5$ V/Å. The topological protection of two-domain metastable configurations within the xy plane is overcome through out-of-plane rotations of the local Mn moments towards the z axis, effectively enabling transitions through the third spatial dimension. Figures 8(d) and 8(e) show the transition states between the two-domain configurations and the AF ground state at $E_y = 0.5$ V/Å. These TS are nearly the mirror image of each other, differing only in their chirality. The associated relaxation mechanisms along the MEP are also very similar. The same behavior is observed for $E_y = 0$, as shown in Fig. 9(c).

In the field-free case, the first excited states in PtFePt and PtMnPt stripes are twofold degenerate with $\eta_z = \pm 1$ because of inversion symmetry. By applying E_y, the degeneracy is lifted, yet both states remain locally stable for the field strengths considered in this paper ($E_y \leqslant 0.5$ V/Å). However, at larger fields or in materials with stronger DM couplings, it is theoretically possible that the excited state with the unfavorable chirality becomes unstable. As already discussed,

the energy barriers separating the two-domain metastable states from the ground state are overcome through rotations of the local moments out of the xy plane toward the z axis, i.e., through the third spatial dimension. In the case of the two-domain state with unfavorable chirality, the sum of the local anisotropy energies and symmetric exchange energies increases, while the DM energy, being positive, decreases along this escape path. Therefore, as long as the energy increase from the local anisotropies and exchange interactions outweighs the DM-energy gain, this excited configuration remains metastable. In any case, the role of the DM couplings is evident from the fact that the downhill energy barrier away from the two-domain state with unfavorable chirality is smaller than the barrier stabilizing the two-domain state with favorable chirality (see Figs. 7 and 10).

V. CONCLUSIONS

First-principles electronic calculations and classical spin modeling have been combined to characterize the magnetic interactions and energy landscapes of PtFePt and PtMnPt stripes, which are representative examples of one-dimensional $3d$-$5d$ alloys of fundamental and technological interest. Special attention has been given to the possibilities of manipulating the magnetic behavior through static external electric fields. To this end, the frozen-magnon dispersion relations of the stripes have been calculated within the framework of density-functional theory by considering spiral SDWs with varying wave numbers, spin-polarization planes, and chiralities. In this way, the stability of the ground-state configurations and the material-specific energy changes resulting from variations in the magnetic order have been quantified. Subsequently, the effective interactions between the magnetic moments and the local anisotropy energies at the $3d$ atoms have been derived, including their dependence on an applied EF. Using these magnetic interactions, a classical spin Hamiltonian has been constructed, suitable for systematic exploration of the energy landscapes of the stripes as a function of the orientations of the local magnetic moments. The stable and metastable magnetic configurations, as well as the transition states connecting them, have been determined without imposing any symmetry constraints. The relative stability, energy barriers, and morphology of the critical configurations have been analyzed, and the mechanisms for the creation, annihilation, and translation of magnetic domains have been identified by calculating the minimum energy paths connecting the corresponding local minima. In this way, the significance of topological protection for the stability of MDs has been identified and the nearly barrierless mobility of MDs along the stripes has been demonstrated. Moreover, the roles played by the various types of magnetic interactions (i.e., isotropic, symmetric anisotropic, and antisymmetric anisotropic) in defining the magnetic configurations of the metastable and transition states has been analyzed from a local perspective. Finally, the properties of FM PtFePt and AF PtMnPt have been contrasted.

The present study suggests several fruitful research directions and theoretical developments. On the one hand, it would be very interesting to apply the present combination of first-principles electronic theory and energy-landscape characterization to two-dimensional nanostructures, such as ultrathin films and multilayers, where a much wider variety of metastable spin textures have been observed and far more complex energy landscapes can be readily expected. Furthermore, it would be important to contrast the properties of free-standing or weakly interacting stripes with those of stripes deposited on metal surfaces. Indeed, in the case of deposited nanostructures, inversion symmetry is already broken by the substrate, implying the presence of some degree of DM interactions. Applying EFs should result in potentially significant changes in the size and orientations of the DM vectors, with concomitant changes in the favored spin-polarization planes and chiralities.

On the other hand, from a methodological perspective, the present theory should be further developed to quantify the temperature dependence of the effective magnetic couplings and to characterize any possible temperature-induced changes in the metastable magnetic configurations. Particular attention should be given to the magneto-anisotropic properties, which are known to be very sensitive to spin and electronic excitations, often at temperatures well below those that significantly break long-range spin correlations [3–6,18–21]. As a first step, it would be interesting to apply the spin model derived in this paper to assess the effects of spin fluctuations on the metastable magnetic orders and their relative stability, assuming for simplicity that the interaction parameters are temperature independent. Accounting for Gaussian fluctuations of the magnetic configurations around the local minima and performing unconstrained Monte Carlo simulations would allow us to determine the temperature-dependent energy and entropy associated with spin fluctuations, including anisotropy and chirality effects. Moreover, the temperature dependence of transition rates between the various metastable states could be quantified, for example, in the framework of transition-state theory [94].

In parallel, it would be worthwhile to perform electronic DFT calculations for representative nonperiodic spin configurations (e.g., involving flipped single spins or short-range-order domains) to test the transferability of the interaction parameters to arbitrary disordered-local-moment situations, beyond the periodic SDWs considered in this work. A further challenging perspective is to investigate the dependence of the effective magnetic interactions on the electronic temperature. While the isotropic Heisenberg couplings in TM wires and monolayers have been shown to be rather insensitive to electronic heating [104], very little is currently know about the trends concerning SO effects such as local anisotropy, exchange anisotropy, and DM interactions. In fact, recent model calculations for Ni monolayers [21] have shown that the Stoner electron-hole excitations play a central role in the experimentally observed temperature-induced reorientation transition from perpendicular to in-plane magnetization in ultrathin Ni films [3–6].

Finally, it would be most worthwhile to extend the present investigations to study the dynamics of magnetic order in PtFePt and PtMnPt stripes under the action of time-dependent magnetic fields and current pulses, according to the Landau-Lifshitz-Gilbert equation and related models [105–108]. In this context, a characterization of the magnetic energy landscapes is expected to be highly useful, both as a preliminary

study and as a tool for interpreting the dynamics. From these perspectives, the present investigations may serve as a blueprint for achieving a more detailed understanding of the local-environment dependence of the interactions between magnetic moments, their role in collective responses and relaxation processes, and the energy landscapes that underlie the physics of complex magnetic nanostructures.

ACKNOWLEDGMENTS

The authors gratefully acknowledge computing resources provided by the IT Service Center of the University of Kassel, the Center for Scientific Computing of the Goethe University Frankfurt, and the National High Performance Computing Center for Computational Engineering Science at the Technical University of Darmstadt.

DATA AVAILABILITY

The data that support the findings of this article are not publicly available. The data are available from the authors upon reasonable request.

APPENDIX: MODEL ANISOTROPY AND INTERACTION RANGE

The explicit definition of the model given by Eqs. (1)–(7) involves a physically motivated compromise between achieving the best fit of the first principles calculations and avoiding unrealistic overfitting. To identify the relevant type of anisotropy and the spatial range of the interactions we have applied the Akaike information criterion (AIC) including the correction for small sample sizes. The corresponding quality measure Q is given by

$$Q = n \ln\left(\sigma_z^2/n\right) + 2k + \frac{2k(k+1)}{n-k-1}, \tag{A1}$$

where n is the number of data points, k is the number of considered parameters in the model, and σ_z^2 is the sum of the squared residuals divided by the band width of the dispersion relation [84,85,109]. According to the AIC, the smaller the value of Q, the more reliable the fitting of the dataset is [84].

TABLE II. Quality measure Q for models having isotropic exchange interactions Iso_ν and anisotropic exchange interactions Ani_ν, where ν indicates the considered number of nearest neighbors. The values correspond to the dispersion relations for an electric field $E_y = 0.5$ V/Å and, in brackets, for $E_y = 0$.

Model	PtFePt	PtMnPt	Average
Iso_2	75.6 (78.2)	58.3 (65.8)	69.5
Iso_3	75.7 (79.3)	60.4 (68.2)	70.9
Iso_4	79.0 (71.0)	64.7 (71.2)	71.5
Ani_2	83.1 (79.3)	26.0 (50.3)	59.7
Ani_3	95.3 (95.9)	18.5 (61.2)	67.7
Ani_4	124.3 (108.3)	47.5 (88.9)	92.3

To find the most appropriate model describing the data obtained from the DFT calculations, different types of anisotropies and interaction ranges have been considered. Models with isotropic exchange interactions are labeled as Iso_ν, where ν stands for the range of the exchange interaction, i.e., up to second ($\nu = 2$), third ($\nu = 3$), or fourth ($\nu = 4$) nearest neighbors. Models with anisotropic exchange interactions are denoted as Ani_ν. The calculated Q values are shown in Table II. One observes that the Ani_2 model yields the smallest average Q, making it the most appropriate model for describing the DFT results according to this criterion.

[1] J. G. Gay and R. Richter, Spin anisotropy of ferromagnetic films, Phys. Rev. Lett. **56**, 2728 (1986).
[2] P. Bruno, Tight-binding approach to the orbital magnetic moment and magnetocrystalline anisotropy of transition-metal monolayers, Phys. Rev. B **39**, 865(R) (1989).
[3] D. P. Pappas, K.-P. Kämper, and H. Hopster, Reversible transition between perpendicular and in-plane magnetization in ultrathin films, Phys. Rev. Lett. **64**, 3179 (1990).
[4] C. S. Arnold, D. P. Pappas, and A. P. Popov, Second- and first-order phase transitions in the magnetic reorientation of ultrathin Fe on Gd, Phys. Rev. Lett. **83**, 3305 (1999).
[5] R. Allenspach and A. Bischof, Magnetization direction switching in Fe/Cu(100) epitaxial films: Temperature and thickness dependence, Phys. Rev. Lett. **69**, 3385 (1992).
[6] N. Saratz, A. Lichtenberger, O. Portmann, U. Ramsperger, A. Vindigni, and D. Pescia, Experimental phase diagram of perpendicularly magnetized ultrathin ferromagnetic films, Phys. Rev. Lett. **104**, 077203 (2010).
[7] B. N. Engel, M. H. Wiedman, and C. M. Falco, Overlayer-induced perpendicular anisotropy in ultrathin Co films, J. Appl. Phys. **75**, 6401 (1994).
[8] J. Kohlhepp and U. Gradmann, Magnetic surface anisotropies of Co(0001)-based interfaces from in situ magnetometry of Co films on Pd(111) covered with ultrathin films of Pd and Ag, J. Magn. Magn. Mater. **139**, 347 (1995).
[9] G. M. Pastor, J. Dorantes-Dávila, S. Pick, and H. Dreyssé, Magnetic anisotropy of 3*d* transition-metal clusters, Phys. Rev. Lett. **75**, 326 (1995).
[10] R. K. Kawakami, E. J. Escorcia-Aparicio, and Z. Q. Qiu, Symmetry-induced magnetic anisotropy in Fe films frown on stepped Ag(001), Phys. Rev. Lett. **77**, 2570 (1996).
[11] J. Dorantes-Dávila and G. M. Pastor, In-plane magnetic anisotropy of ultrahin bcc (110) transition-metal films, Phys. Rev. Lett. **77**, 4450 (1996).
[12] J. Dorantes-Dávila and G. M. Pastor, Magnetic anisotropy of one-dimensional nanostructures of transition metals, Phys. Rev. Lett. **81**, 208 (1998).
[13] S. Boukari, E. Beaurepaire, H. Bulou, B. Carrière, J. P. Deville, F. Scheurer, M. Desantis, and R. Baudoing-Savois, Influence of strain on the magnetocrystalline anisotropy in epitaxial Cr/Co/Pd(111) films, Phys. Rev. B **64**, 144431 (2001).
[14] P. Gambardella, A. Dallmeyer, K. Maiti, M. C. Malagoli, W. Eberhardt, K. Kern, and C. Carbone, Ferromagnetism in

one-dimensional monatomic metal chains, Nature (London) **416**, 301 (2002).

[15] P. Gambardella, S. Rusponi, M. Veronese, S. S. Dhesi, C. Grazioli, A. Dallmeyer, I. Cabria, R. Zeller, P. H. Dederichs, K. Kern, C. Carbone, and H. Brune, Giant magnetic anisotropy of single cobalt atoms and nanoparticles, Science **300**, 1130 (2003).

[16] J. Dorantes-Dávila and G. M. Pastor, Magnetic reorientation transitions along the crossover from one-dimensional to two-dimensional transition-metal nanostructures, Phys. Rev. B **72**, 085427 (2005).

[17] N. N. Negulyaev, J. Dorantes-Dávila, L. Niebergall, L. Juárez-Reyes, G. M. Pastor, and V. S. Stepanyuk, Alloying route to tailor giant magnetic anisotropy in transition-metal nanowires, Phys. Rev. B **87**, 054425 (2013).

[18] J. B. Staunton, S. Ostanin, S. S. A. Razee, B. L. Gyorffy, L. Szunyogh, B. Ginatempo, and E. Bruno, Temperature dependent magnetic anisotropy in metallic magnets from an *ab initio* electronic structure theory: $L1_0$-ordered FePt, Phys. Rev. Lett. **93**, 257204 (2004).

[19] A. Buruzs, P. Weinberger, L. Szunyogh, L. Udvardi, P. I. Chleboun, A. M. Fischer, and J. B. Staunton, *Ab initio* theory of temperature dependence of magnetic anisotropy in layered systems: Applications to thin Co films on Cu(100), Phys. Rev. B **76**, 064417 (2007).

[20] I. A. Zhuravlev, V. P. Antropov, and K. D. Belashchenko, Spin-fluctuation mechanism of anomalous temperature dependence of magnetocrystalline anisotropy in itinerant magnets, Phys. Rev. Lett. **115**, 217201 (2015).

[21] J. Dorantes-Dávila, R. Garibay-Alonso, and G. M. Pastor, Spin-fluctuation theory of temperature-driven spin reorientations in ferromagnetic transition metal thin films, Phys. Rev. B **110**, 174406 (2024).

[22] A. Fert and P. M. Levy, Role of anisotropic exchange interactions in determining the properties of spin-glasses, Phys. Rev. Lett. **44**, 1538 (1980).

[23] V. Kashid, T. Schena, B. Zimmermann, Y. Mokrousov, S. Blügel, V. Shah, and H. G. Salunke, Dzyaloshinskii-Moriya interaction and chiral magnetism in $3d$-$5d$ zigzag chains: Tight-binding model and *ab initio* calculations, Phys. Rev. B **90**, 054412 (2014).

[24] H. Yang, A. Thiaville, S. Rohart, A. Fert, and M. Chshiev, Anatomy of Dzyaloshinskii-Moriya interaction at Co/Pt interfaces, Phys. Rev. Lett. **115**, 267210 (2015).

[25] A. A. Khajetoorians, M. Steinbrecher, M. Ternes, M. Bouhassoune, M. dos Santos Dias, S. Lounis, J. Wiebe, and R. Wiesendanger, Tailoring the chiral magnetic interaction between two individual atoms, Nat. Commun. **7**, 10620 (2016).

[26] A. Belabbes, G. Bihlmayer, F. Bechstedt, S. Blügel, and A. Manchon, Hund's rule-driven Dzyaloshinskii-Moriya interaction at $3d$−$5d$ interfaces, Phys. Rev. Lett. **117**, 247202 (2016).

[27] B. Schweflinghaus, B. Zimmermann, M. Heide, G. Bihlmayer, and S. Blügel, Role of Dzyaloshinskii-Moriya interaction for magnetism in transition-metal chains at Pt step edges, Phys. Rev. B **94**, 024403 (2016).

[28] M. Perini, S. Meyer, B. Dupé, S. von Malottki, A. Kubetzka, K. von Bergmann, R. Wiesendanger, and S. Heinze, Domain walls and Dzyaloshinskii-Moriya interaction in epitaxial Co/Ir(111) and Pt/Co/Ir(111), Phys. Rev. B **97**, 184425 (2018).

[29] H. Yang, J. Liang, and Q. Cui, First-principles calculations for Dzyaloshinskii–Moriya interaction, Nat. Rev. Phys. **5**, 43 (2023).

[30] B. Jang, S. Riemer, and G. M. Pastor, Chiral magnetic interactions in small Fe clusters triggered by symmetry-breaking adatoms, Symmetry **15**, 397 (2023).

[31] B. Jang and G. M. Pastor, Reversible electric field manipulation of the Dzyaloshinskii-Moriya interactions in transition metal dimers, Phys. Rev. B **110**, 014443 (2024).

[32] I. Dzyaloshinsky, A Thermodynamic Theory of "weak" ferromagnetism of antiferromagnetics, J. Phys. Chem. Solids **4**, 241 (1958).

[33] T. Moriya, Anisotropic superexchange interaction and weak ferromagnetism, Phys. Rev. **120**, 91 (1960).

[34] T. Moriya, New mechanism of anisotropic superexchange interaction, Phys. Rev. Lett. **4**, 228 (1960).

[35] M. Bode, M. Heide, K. von Bergmann, P. Ferriani, S. Heinze, G. Bihlmayer, A. Kubetzka, O. Pietzsch, S. Blügel, and R. Wiesendanger, Chiral magnetic order at surfaces driven by inversion asymmetry, Nature (London) **447**, 190 (2007).

[36] S. Polesya, S. Mankovsky, S. Bornemann, D. Ködderitzsch, J. Minár, and H. Ebert, Skyrmion magnetic structure of an ordered FePt monolayer deposited on Pt(111), Phys. Rev. B **89**, 184414 (2014).

[37] M. Perini, S. Meyer, A. Kubetzka, R. Wiesendanger, S. Heinze, and K. von Bergmann, Electrical detection of domain walls and skyrmions in Co films using noncollinear magnetoresistance, Phys. Rev. Lett. **123**, 237205 (2019).

[38] R. E. Camley and K. L. Livesey, Consequences of the Dzyaloshinskii-Moriya interaction, Surf. Sci. Rep. **78**, 100605 (2023).

[39] D. Rahmedov, D. Wang, J. Íñiguez, and L. Bellaiche, Magnetic cycloid of $BiFeO_3$ from atomistic simulations, Phys. Rev. Lett. **109**, 037207 (2012).

[40] H. Katsura, N. Nagaosa, and A. V. Balatsky, Spin current and magnetoelectric effect in noncollinear magnets, Phys. Rev. Lett. **95**, 057205 (2005).

[41] S. Meyer, B. Xu, M. J. Verstraete, L. Bellaiche, and B. Dupé, Spin-current driven Dzyaloshinskii-Moriya interaction in multiferroic $BiFeO_3$ from first principles, Phys. Rev. B **108**, 024403 (2023).

[42] L. Desplat, S. Meyer, J. Bouaziz, P. M. Buhl, S. Lounis, B. Dupé, and P.-A. Hervieux, Mechanism for ultrafast electric-field driven skyrmion nucleation, Phys. Rev. B **104**, L060409 (2021).

[43] A. Deka, B. Rana, R. Anami, K. Miura, H. Takahashi, Y. C. Otani, and Y. Fukuma, Electric-field control of interfacial in-plane magnetic anisotropy in CoFeB/MgO junctions, Phys. Rev. B **101**, 174405 (2020).

[44] A. Rajanikanth, T. Hauet, F. Montaigne, S. Mangin, and S. Andrieu, Magnetic anisotropy modified by electric field in V/Fe/MgO(001)/Fe epitaxial magnetic tunnel junction, Appl. Phys. Lett. **103**, 062402 (2013).

[45] D. Preziosi, M. Alexe, D. Hesse, and M. Salluzzo, Electric-field control of the orbital occupancy and magnetic moment of a transition-metal oxide, Phys. Rev. Lett. **115**, 157401 (2015).

[46] W. Zhang, H. Zhong, R. Zang, Y. Zhang, S. Yu, G. Han, G. L. Liu, S. S. Yan, S. Kang, and L. M. Mei, Electrical field enhanced interfacial Dzyaloshinskii-Moriya interaction in MgO/Fe/Pt system, Appl. Phys. Lett. **113**, 122406 (2018).

[47] T. Koyama, Y. Nakatani, J. Ieda, and D. Chiba, Electric field control of magnetic domain wall motion via modulation of the Dzyaloshinskii-Moriya interaction, Sci. Adv. **4**, eaav0265 (2018).

[48] M. Rafique, A. Herklotz, K. Dörr, and S. Manzoor, Reversible electric-field-driven magnetization in a columnar nanocomposite film, Thin Solid Films **685**, 47 (2019).

[49] Y. Ba, S. Zhuang, Y. Zhang, Y. Wang, Y. Gao, H. Zhou, M. Chen, W. Sun, Q. Liu, G. Chai, *et al.*, Electric-field control of skyrmions in multiferroic heterostructure via magnetoelectric coupling, Nat. Commun. **12**, 322 (2021).

[50] H. Terada, S. Ohya, L. D. Ahn, Y. Iwasa, and M. Tanada, Magnetic anisotropy control by applying an electric field to the side surface of ferromagnetic films, Sci. Rep. **7**, 5618 (2017).

[51] H. Mizuno, T. Moriyama, K. Tanaka, K. Kawaguchi, K. T., D. Chiba, and T. Ono, Electric field effect on spectroscopic g-factor and magnetic anisotropy in a Pt/Co/MgO ultrathin film, Jpn. J. Appl. Phys. **61**, 103001 (2022).

[52] B. Dai, D. Wu, S. A. Razavi, S. Xu, H. He, Q. Shu, M. Jackson, F. Mahfouzi, H. Huang, Q. Pan, *et al.*, Electric field manipulation of spin chirality and skyrmion dynamic, Sci. Adv. **9**, eade6836 (2023).

[53] X. Xue, Z. Zhou, B. Peng, M. Zhu, Y. Zhang, W. Ren, T. Ren, X. Yang, T. Nan, N. X. Sun, and M. Liu, Electric field induced reversible 180° magnetization switching through tuning of interfacial exchange bias along magnetic easy-axis in multiferroic laminates, Sci. Rep. **5**, 16480 (2015).

[54] A. Sonntag, J. Hermenau, A. Schlenhoff, J. Friedlein, S. Krause, and R. Wiesendanger, Electric-field-induced magnetic anisotropy in a nanomagnet investigated on the atomic scale, Phys. Rev. Lett. **112**, 017204 (2014).

[55] P.-J. Hsu, A. Kubetzka, A. Finco, N. Romming, K. von Bergmann, and R. Wiesendanger, Electric-field-driven switching of individual magnetic skyrmions, Nat. Nanotechnol. **12**, 123 (2017).

[56] K. Nakamura, R. Shimabukuro, Y. Fujiwara, T. Akiyama, T. Ito, and A. J. Freeman, Giant modification of the magnetocrystalline anisotropy in transition-metal monolayers by an external electric field, Phys. Rev. Lett. **102**, 187201 (2009).

[57] J. Hu and R. Wu, Control of the magnetism and magnetic anisotropy of a single-molecule magnet with an electric field, Phys. Rev. Lett. **110**, 097202 (2013).

[58] M. Tsujikawa and T. Oda, Finite electric field effects in the large perpendicular magnetic anisotropy surface Pt/Fe/Pt(001): A first-principles study, Phys. Rev. Lett. **102**, 247203 (2009).

[59] M. Tanveer, J. Dorantes-Dávila, and G. M. Pastor, Reversible electric-field manipulation of the adsorption morphology and magnetic anisotropy of small Fe and Co clusters on graphene, Phys. Rev. B **96**, 224413 (2017).

[60] B. Pradines, B. Cahier, N. Suaud, and N. Guihéry, Impact of the electric field on isotropic and anisotropic spin Hamiltonian parameters, J. Chem. Phys. **157**, 204308 (2022).

[61] N. N. Negulyaev, V. S. Stepanyuk, W. Hergert, and J. Kirschner, Electric field as a switching tool for magnetic states in atomic-scale nanostructures, Phys. Rev. Lett. **106**, 037202 (2011).

[62] E. Torun, H. Sahin, C. Bacaksiz, R. T. Senger, and F. M. Peeters, Tuning the magnetic anisotropy in single-layer crystal structures, Phys. Rev. B **92**, 104407 (2015).

[63] X. Z. Yu, Y. Onose, N. Kanazawa, J. H. Park, J. H. Han, Y. Matsui, N. Nagaosa, and Y. Tokura, Real-space observation of a two-dimensional skyrmion crystal, Nature (London) **465**, 901 (2010).

[64] M. Oba, K. Nakamura, T. Akiyama, T. Ito, M. Weinert, and A. J. Freeman, Electric-field-induced modification of the magnon energy, exchange interaction, and Curie temperature of transition-metal thin films, Phys. Rev. Lett. **114**, 107202 (2015).

[65] M. A. Goerzen, S. von Malottki, G. J. Kwiatkowski, P. F. Bessarab, and S. Heinze, Atomistic spin simulations of electric-field-assisted nucleation and annihilation of magnetic skyrmions in Pd/Fe/Ir(111), Phys. Rev. B **105**, 214435 (2022).

[66] S. Paul and S. Heinze, Electric-field driven stability control of skyrmions in an ultrathin transition-metal film, npj Comput. Mater. **8**, 105 (2022).

[67] J. Hubbard, The magnetism of iron, Phys. Rev. B **19**, 2626 (1979).

[68] H. Hasegawa, Single-siet spin Ffluctuation theory of itinerant-electron systems with narrow bands, J. Phys. Soc. Jpn. **49**, 178 (1980).

[69] R. Garibay-Alonso, J. Dorantes-Dávila, and G. M. Pastor, Finite-temperature magnetism of Ni monolayers: Interplay between flips and amplitude fluctuations of the local moments, Phys. Rev. B **85**, 224409 (2012).

[70] L. Udvardi, L. Szunyogh, K. Palotás, and P. Weinberger, First-principles relativistic study of spin waves in thin magnetic films, Phys. Rev. B **68**, 104436 (2003).

[71] P. Hohenberg and W. Kohn, Inhomogeneous electron gas, Phys. Rev. **136**, B864 (1964).

[72] W. Kohn and L. J. Sham, Self-consistent equations including exchange and correlation effects, Phys. Rev. **140**, A1133 (1965).

[73] G. Kresse and J. Furthmüller, Efficiency of *ab-initio* total energy calculations for metals and semiconductors using a plane-wave basis set, Comput. Mater. Sci. **6**, 15 (1996).

[74] G. Kresse and D. Joubert, From ultrasoft pseudopotentials to the projector augmented-wave method, Phys. Rev. B **59**, 1758 (1999).

[75] P. E. Blöchl, Projector augmented-wave method, Phys. Rev. B **50**, 17953 (1994).

[76] J. P. Perdew, K. Burke, and M. Ernzerhof, Generalized gradient approximation made simple, Phys. Rev. Lett. **77**, 3865 (1996).

[77] D. Hobbs, G. Kresse, and J. Hafner, Fully unconstrained noncollinear magnetism within the projector augmented-wave method, Phys. Rev. B **62**, 11556 (2000).

[78] P. D. Haynes and M. C. Payne, Corrected penalty-functional method for linear-scaling calculations within density-functional theory, Phys. Rev. B **59**, 12173 (1999).

[79] G. Kresse, M. Marsman, and J. Furthmüller, VASP Manual (2016) http://www.vasp.at/wiki/The_VASP_Manual.

[80] S. Steiner, S. Khmelevskyi, M. Marsmann, and G. Kresse, Calculation of the magnetic anisotropy with projected-augmented-wave methodology and the case study of disordered $Fe_{1-x}Co_x$ alloys, Phys. Rev. B **93**, 224425 (2016).

[81] B. L. Gyorffy, A. J. Pindor, J. Staunton, G. M. Stocks, and H. Winter, A first-principles theory of ferromagnetic phase transitions in metals, J. Phys. F: Met. Phys. **15**, 1337 (1985).

[82] L. Thomas and S. Parkin, Current induced domain-wall motion in magnetic nanowires, in *Handbook of Magnetism and Advanced Magnetic Materials* (John Wiley & Sons, Hoboken, NJ, 2007) pp. 282–302.

[83] Multiple tests have been performed to assess the numerical accuracy of our calculations of the spin-wave energies $\mathcal{E}^{\alpha}_{\delta\gamma}(q)$, particularly for $\delta\gamma = xy$ and finite electric field $E_y = 0.5\,\mathrm{V/Å}$, where the dependence on chirality $\alpha = \pm 1$ is significant. For example, varying the cutoff energy in the range $500\,\mathrm{eV} \leqslant E_{\max} \leqslant 750\,\mathrm{eV}$, the number of k points in the range in the range $60 \leqslant N_k \leqslant 180$, and the convergence criterion for the total energy per atom in the range $10^{-5}\,\mathrm{eV} \geqslant E_{\mathrm{diff}} \geqslant 10^{-7}\,\mathrm{eV}$ shows that the energy differences yielding the nearest-neighbor DM interactions and the local anisotropy energies are converged within 0.1 meV. This value corresponds to the uncertainty associated with fitting the dispersion relations and is therefore sufficient for our purposes.

[84] H. Akaike, A new look at the statistical model identification, IEEE Trans. Automat. Contr. **19**, 716 (1974).

[85] N. Sugiura, Further analysis of the data by Akaike's information criterion and the finite corrections, Commun. Stat. - Theory Methods **7**, 13 (1978).

[86] M. R. Hestenes and E. Stiefel, Methods of conjugate gradients for solving linear systems, J. Res. Natl. Bur. Stand. **49**, 409 (1952).

[87] R. Fletcher and C. M. Reeves, Function minimization by conjugate gradients, Comput. J. **7**, 149 (1964).

[88] L. Armijo, Minimization of functions having Lipschitz continuous first partial derivatives, Pac. J. Math. **16**, 1 (1966).

[89] J. Nocedal and S. J. Wright, *Numerical Optimization*, 2nd ed. (Springer, New York, 2006).

[90] P.-A. Absil, R. Mahony, and R. Sepulchre, *Optimization Algorithms on Matrix Manifolds* (Princeton University Press, Princeton, NJ, 2008).

[91] N. Boumal, *An introduction to Optimization on Smooth Manifolds* (Cambridge University Press, Cambridge, 2023).

[92] H. Jónsson, G. Mills, and K. W. Jacobsen, Nudged elastic band method for finding minimum energy paths of transitions, in *Classical and Quantum Dynamics in Condensed Phase Simulations*, edited by B. J. Berne, G. Ciccotti, and D. F. Coker (World Scientific, Singapore, 1998), pp. 385–404.

[93] G. Henkelman and H. Jónsson, Improved tangent estimate in the nudged elastic band method for finding minimum energy paths and saddle points, J. Chem. Phys. **113**, 9978 (2000).

[94] P. F. Bessarab, V. M. Uzdin, and H. Jónsson, Method for finding mechanism and activation energy of magnetic transitions, applied to skyrmion and antivortex annihilation, Comput. Phys. Commun. **196**, 335 (2015).

[95] C. J. Cerjan and W. H. Miller, On finding transition states, J. Chem. Phys. **75**, 2800 (1981).

[96] L. J. Munro and D. J. Wales, Defect migration in crystalline silicon, Phys. Rev. B **59**, 3969 (1999).

[97] M. Tanveer, P. Ruiz-Díaz, and G. M. Pastor, Electronic and magnetic properties of spiral spin-density-wave states in transition-metal chains, Phys. Rev. B **94**, 094403 (2016).

[98] The DFT calculations reproduce the symmetry constraints $p^{0,z}_{-} = p^{0,z}_{+} = 0$, $p^{0,y}_{+} = -p^{0,y}_{-}$, and $p^{0,x}_{-} = p^{0,x}_{+}$ within numerical accuracy, which is estimated to be of the order of $10^{-5}\mathrm{e\,Å}$. Notice that the dipole moments $p^{0,x}_{+} = p^{0,x}_{-}$ along the bond connecting the Fe atoms need not be zero, since the SDWs break the reflection symmetry across the plane passing perpendicularly through the middle of the vector connecting the Fe atoms. Their values are typically one or two orders of magnitude smaller than the DM-relevant chiral component. In all circumstances, $p^{0,x}$ has no effect on the DM coupling because it is independent of chirality.

[99] M. Z. Hasan and C. L. Kanse, *Colloquium*: Topological insulators, Rev. Mod. Phys. **82**, 3045 (2010).

[100] N. Nagaosa and Y. Tokura, Topological properties and dynamics of magnetic skyrmions, Nat. Nanotechnol. **8**, 899 (2013).

[101] A. Thiaville and J. Miltat, Topology and magnetic domain walls, in *Topology in Magnetism*, edited by J. Zang, V. Cros, and A. Hoffmann (Springer International Publishing, New York, 2018), pp. 41–73.

[102] S. S. P. Parkin, M. Hayashi, and L. Thomas, Magnetic domain-wall racetrack memory, Science **320**, 190 (2008).

[103] G. S. D. Beach, C. Nistor, C. Knutson, M. Tsoi, and J. L. Erskine, Dynamics of field-driven domain-wall propagation in ferromagnetic nanowires, Nat. Mater. **4**, 741 (2005).

[104] W. Töws and G. M. Pastor, Theoretical study of the temperature dependence of the magnon dispersion relation in transition-metal wires and monolayers, Phys. Rev. B **86**, 054443 (2012).

[105] L. D. Landau and E. M. Lifshitz, On the theory of the dispersion of magnetic permeability in ferromagnetic bodies, Phys. Z. Sowjet. **8**, 153 (1935).

[106] T. L. Gilbert, A phenomenological theory of damping in ferromagnetic materials, IEEE Trans. Magn. **40**, 3443 (2004).

[107] J. C. Slonczewski, Current-driven excitation of magnetic multilayers, J. Magn. Magn. Mater. **159**, L1 (1996).

[108] A. Brataas, A. D. Kent, and H. Ohno, Current-induced torques in magnetic materials, Nat. Mater. **11**, 372 (2012).

[109] C. M. Hurvich and C. L. Tsai, Regression and time series model selection in small samples, Biometrika **76**, 297 (1989).